

Improving time-delay cosmography with spatially resolved kinematics

Anowar J. Shajib,¹[★] Tommaso Treu¹ and Adriano Agnello²

¹*Department of Physics and Astronomy, University of California, Los Angeles, CA 90095-1547, USA*

²*European Southern Observatory, Karl-Schwarzschild-Strasse 2, 85748 Garching bei München, DE*

Accepted 2017 September 04. Received 2017 September 04; in original form 2017 February 14

ABSTRACT

Strongly gravitational lensed quasars can be used to measure the so-called time-delay distance $D_{\Delta t}$, and thus the Hubble constant H_0 and other cosmological parameters. Stellar kinematics of the deflector galaxy play an essential role in this measurement by: i) helping break the mass-sheet degeneracy; ii) determining in principle the angular diameter distance D_d to the deflector and thus further improving the cosmological constraints. In this paper we simulate observations of lensed quasars with integral field spectrographs and show that spatially resolved kinematics of the deflector enable further progress by helping break the mass-anisotropy degeneracy. Furthermore, we use our simulations to obtain realistic error estimates with current/upcoming instruments like OSIRIS on Keck and NIRSPEC on the James Webb Space Telescope for both distances (typically $\sim 6\%$ on $D_{\Delta t}$ and $\sim 10\%$ on D_d). We use the error estimates to compute cosmological forecasts for the sample of nine lenses that currently have well measured time delays and deep Hubble Space Telescope images and for a sample of 40 lenses that is projected to be available in a few years through follow-up of candidates found in ongoing wide field surveys. We find that H_0 can be measured with 2%(1%) precision from nine(40) lenses in a flat Λ CDM cosmology. We study several other cosmological models beyond the flat Λ CDM model and find that time-delay lenses with spatially resolved kinematics can greatly improve the precision of the cosmological parameters measured by cosmic microwave background data.

Key words: gravitational lensing: strong – cosmological parameters – methods: numerical

1 INTRODUCTION

Our current understanding of cosmography, i.e. the description of geometry and kinematics of the universe, has been largely acquired from the measurements of cosmic distances as a function of redshift. For example, relative luminosity distance measurements using type Ia supernovae led to the discovery of dark energy (Riess et al. 1998; Perlmutter et al. 1999). More recently, baryon acoustic oscillation (BAO) in galaxy clustering has been used to determine angular diameter distances as a function of redshifts (Eisenstein et al. 2005; Alam et al. 2016).

Absolute distances, and the Hubble constant H_0 in particular, play a central role in cosmography. In fact, the uncertainty on H_0 is currently one of the main limiting factors in cosmological inferences based on the cosmic microwave background (CMB; e.g. Suyu et al. 2012; Weinberg et al. 2013). The tension between the recent measurement of the

local value of H_0 to 2.4% precision determined from type Ia supernovae (Riess et al. 2016; Bernal et al. 2016), and that extrapolated from the CMB assuming a flat Λ Cold Dark Matter (Λ CDM) cosmology highlights the importance of absolute distances. If the tension cannot be explained as residual systematic uncertainties in one (or both) measurements, it may be an indication of new physics, like additional families of relativistic particles, departures from flatness, or dark energy that is not the cosmological constant (Riess et al. 2016). In this context, independent and precise measurements of absolute distances are needed to resolve this tension, and may be required in order to disprove conclusively the standard flat Λ CDM model.

Gravitational lens systems where the source is variable in time provide a powerful direct measurement of distances, that is completely independent of the local distance ladder and the CMB (Refsdal 1964). Substantial progress in data quality, monitoring campaigns, and modeling techniques over the past decade have finally allowed this technique to deliver on its promises (see Treu & Marshall 2016,

[★] E-mail: ajshajib@astro.ucla.edu

for a historical perspective and a review of current methods). It has recently been shown that just three lenses are sufficient to determine H_0 to 3.8% precision (e.g. Suyu et al. 2010, 2013; Bonvin et al. 2017), in Λ CDM.

The primary distance measurement is the so-called time-delay distance $D_{\Delta t}$, a multiplicative combination of the three angular diameter distances between the observer, the deflector, and the source. By combining the time-delay measurement with the stellar velocity dispersion measurements of the deflector, it is possible to measure also the angular diameter distance D_d to the deflector (Grillo et al. 2008; Paraficz & Hjorth 2009; Jee et al. 2015), thereby improving the constraints on the cosmological parameters (Jee et al. 2016).

In order to harness the power of strong lenses to constrain cosmography one needs to break two families of degeneracy. The first one is the mass-sheet degeneracy (MSD; Falco et al. 1985) and its generalizations (Schneider & Sluse 2013, 2014; Xu et al. 2016) that affect the interpretation of lensing observables. Breaking this degeneracy requires making appropriate physical assumptions on the mass profile of the main deflector (Xu et al. 2016) or on the properties of the source (Birrer et al. 2016), measuring the lensing effects along the line of sight (Suyu et al. 2010, 2013; Greene et al. 2013; Sluse et al. 2016; Rusu et al. 2017), and including as much non-lensing information as possible, especially stellar velocity dispersion of the deflector (Treu & Koopmans 2002a; Koopmans et al. 2003; Suyu et al. 2010, 2013, 2014; Wong et al. 2017). The interpretation of stellar velocity dispersion data introduces the second degeneracy, known as the mass-anisotropy degeneracy (see, e.g. van der Marel 1994; Courteau et al. 2014, and references therein), whereby different combinations of mass profiles and stellar orbits can reproduce the same kinematic profiles. This holds especially for elliptical galaxies, which constitute most of the deflectors in strong lens samples. Even though lens galaxies and nearby ellipticals are on average consistent with simple density profiles and modest anisotropy (Koopmans et al. 2009; Barnabè et al. 2011; Agnello et al. 2014a), there are significant system-to-system variations and appreciable systematic uncertainties. Also the exploration of different anisotropy profiles can affect the inference on the mass profile, privileging regions of parameters space where the inferred masses depend weakly on the anisotropy parameters (e.g. at large anisotropy radii, Agnello et al. 2014b), a problem that is exacerbated by kinematic data within the half-light radius. The mass-anisotropy degeneracy is alleviated in the *virial regime* of large apertures (e.g. Treu & Koopmans 2002b; Agnello et al. 2013), so a combination of extended radial coverage and a tight control on systematics can be used to aid cosmography with lensing and stellar dynamics (e.g. Birrer et al. 2016).

Spatially resolved kinematics of galaxy scale lensed quasars is challenging with seeing limited observations, owing to the presence of bright quasar within the typical separation of order arcsecond. Diffraction limited spectroscopy is needed to make progress, either from the ground with the assistance of laser guide star adaptive optics (AO), or from space. Recent advances in AO technology and the imminent launch of the James Webb Space Telescope (JWST) make this kind of measurement feasible, and calls for a detailed investigation of its potential for cosmography.

In this paper, we investigate the improvements to time-delay cosmography that can be expected in the next few years by combining spatially resolved kinematics with lensing data. Unfortunately, state of the art modeling techniques are too computationally expensive at present to carry out a full-blown pixel-based analysis of a large number of mock systems. Thus, in order to keep the computational cost manageable, we develop a framework to simulate and model mock lenses in a simplified and effective manner, but calibrated to yield realistic uncertainties as they would be obtained with a pixel-based analysis. We then apply these techniques to study the precision and accuracy that can be achieved on D_d and $D_{\Delta t}$ per system for plausible observational data quality that can be expected for current (e.g. OSIRIS on Keck, Larkin et al. 2006), imminent (NIRSPEC on JWST), and future (e.g. IRIS on the Thirty Meter Telescope (TMT), Wright et al. 2016) integral field spectrographs. Finally, we use our results on the estimated precision of D_d and $D_{\Delta t}$ to forecast the cosmological precision that can be attained with the current sample of nine lenses for which accurate time delays and deep Hubble Space Telescope (HST) imaging data are available, and for a sample of 40 lenses that is expected to be completed in the next few years by a dedicated follow-up campaign of newly discovered lenses from ongoing wide field imaging surveys (e.g. the STRong lensing Insights into the Dark Energy Survey (STRIDES)¹).

Our work builds upon and extends previous work by Jee et al. (2016) in two important ways. First, we consider spatially resolved kinematics whereas Jee et al. (2016) focused on integrated quantities. As we will show, this aspect allows us to let anisotropy be a free parameter and show that the mass-anisotropy degeneracy can be overcome. Second, rather than assuming a target uncertainty on the two distances $D_{\Delta t}$, D_d (Jee et al. 2016, adopted a fiducial 5% uncertainty on both), we derive them from realistic assumptions about the measurements exploring different scenarios corresponding to variation in data quality, e.g. effect of including kinematics, improved instrumental precision, and observing conditions. We then use these uncertainties to infer the attainable precisions on the cosmological parameters.

The structure of this paper is as follows. In Section 2 we briefly review the strong gravitational lensing formalism and describe the mass models we used to simulate the deflector galaxy mass distribution. In Section 3 we describe the methods to create mock lensing and kinematic data from simulated strong lens systems. We present our results on the precision of the cosmological distances in Section 4 and forecast the cosmological parameter uncertainties in Section 5. We follow that with our discussion about the study and comparison with previous works in Section 6 and the limitations of this work in Section 7. Lastly, we conclude the paper with a summary in Section 8.

2 MODEL INGREDIENTS

Multiply-imaged quasars are ideal candidates for time-delay cosmography as the time delay can be measured by moni-

¹ STRIDES is a Dark Energy Survey Broad External Collaboration; PI: Treu. <http://strides.astro.ucla.edu>

toring quasar variability. The deflector in such a system is usually an elliptical galaxy. In this section, we first present a brief review of the strong gravitational lensing formalism in Section 2.1. Then in Section 2.2 we describe the models we use to simulate realistic deflector mass distributions.

2.1 Strong gravitational lensing

In this subsection, we set the notation by briefly reviewing the theory of strong gravitational lensing (see Schneider et al. 2006, for a detailed description). Let us consider a strong gravitational-lens system with the deflector at the origin and the background source at β . Then, the image positions θ are given by the solutions of the lensing equation

$$\beta = \theta - \alpha(\theta), \quad (1)$$

where $\alpha(\theta) = \nabla_\theta \psi(\theta)$ is the deflection angle and ψ is the deflection potential. The dimensionless quantity convergence κ is defined as $\kappa(\theta) \equiv \Sigma(\theta)/\Sigma_{\text{cr}}$, where $\Sigma(\theta)$ is the projected surface mass density of the deflector and Σ_{cr} is the critical surface density for lensing given by

$$\Sigma_{\text{cr}} = \frac{c^2}{4\pi G} \frac{D_s}{D_d D_{\text{ds}}}, \quad (2)$$

where D_s , D_d , and D_{ds} are the angular diameter distances between the observer and the source, between the observer and the deflector, and between the deflector and the source, respectively. The deflection potential is related to the convergence by the Poisson equation

$$\kappa(\theta) = \frac{1}{2} \nabla_\theta^2 \psi(\theta). \quad (3)$$

The Einstein radius of the lens system is given by the solution of Equation (1) with $\beta = 0$ which is the case where the source lies directly behind the deflector. The Einstein radius can be expressed as

$$\theta_{\text{Ein}} = \sqrt{\frac{4GM(\theta_{\text{Ein}} D_d) D_{\text{ds}}}{c^2 D_s D_d}}, \quad (4)$$

where $M(r)$ is the enclosed mass of the deflector within a radius r .

The time delay between two images is

$$\Delta t_{ij} = \frac{D_{\Delta t}}{c} \left[\frac{1}{2} (\theta_i - \beta)^2 - \frac{1}{2} (\theta_j - \beta)^2 - \psi(\theta_i) + \psi(\theta_j) \right]. \quad (5)$$

Here $D_{\Delta t}$ is the time-delay distance given by

$$D_{\Delta t} = (1 + z_d) \frac{D_s D_d}{D_{\text{ds}}}, \quad (6)$$

where z_d is the redshift of the deflector.

The mass-sheet transformation (MST; Falco et al. 1985)

$$\kappa(\theta) \rightarrow \kappa'(\theta) = (1 - \lambda) + \lambda \kappa(\theta), \quad (7)$$

$$\beta \rightarrow \beta' = \lambda \beta \quad (8)$$

leaves the image positions invariant. The additive term $(1 - \lambda)$ can be internal to the deflector mass distribution affecting the time delay and the velocity dispersion as

$$\begin{aligned} \Delta t' &= \lambda \Delta t, \\ \sigma_*' &= \sqrt{\lambda} \sigma_*. \end{aligned} \quad (9)$$

Furthermore, this additive term can be due to the line-of-sight structures external to the deflector mass distribution, quantified as the external convergence $\kappa_{\text{ext}} = 1 - \lambda_{\text{ext}}$, which only affects the time-delay. Schneider & Sluse (2013) point out that assuming a power-law profile for the deflector mass distribution breaks the MSD as the MST of a power law is not a power law. Therefore, it is necessary to consider more flexible models for the deflector mass distribution or families of mass models connected by the source-position transformation (SPT; Schneider & Sluse 2014) to obtain unbiased measurements of the cosmological parameters.

2.2 Deflector mass model

We need to model the mass distribution of the deflector in order to compute spatially resolved kinematics of the deflector and lensing data of the background source. We require this model to be realistic, yet simple enough to be computationally efficient to create mock data for numerous realizations of a lens system while performing the Bayesian inference. Therefore, for simplicity we assume spherically symmetric mass profiles for the deflector instead of elliptical mass profiles. This assumption simplifies many computational tasks by reducing a number of two-dimensional problems to only one-dimensional, namely the radial, ones. Naturally, real lenses are typically not spherical, so our spherical models are not intended literally, but to be representative of non-spherical models, after marginalization over all the non-spherical parameters. As we shall see in Section 3 we will tune our the uncertainties in our spherical models so as to reproduce effectively the uncertainty of non-spherical models.

Following standard practice (e.g. Treu & Koopmans 2002a; Suyu et al. 2014), we describe the mass distribution of the deflector using two components: dark matter and luminous matter, where the luminous matter resides within a dark matter halo. We choose the Navarro-Frenk-White (NFW) profile (Navarro et al. 1996) for the dark matter distribution and Jaffe profile (Jaffe 1983) for the luminous matter distribution. It is empirically known that the total mass distribution in a galaxy, as a combination of the dark matter and luminous matter distributions, closely follows an isothermal profile, which is a power-law profile with the power-law slope $\gamma \approx 2$ (Treu & Koopmans 2004; Koopmans et al. 2006, 2009; Auger et al. 2010; Dutton & Treu 2014).

2.2.1 NFW profile

The NFW profile describes the mass distribution in the dark matter haloes as suggested by cosmological N -body simulations (Navarro et al. 1996, 1997). The spherical NFW profile has the form

$$\rho(r) = \frac{\rho_s}{(r/r_s)(1 + r/r_s)^2}, \quad (10)$$

where ρ_s and r_s are the scale density and radius, respectively. The convergence κ implied by this mass profile is (Bartelmann 1996)

$$\kappa(\theta) = \frac{2\kappa_s}{(x^2 - 1)} [1 - \mathcal{F}(x)], \quad (11)$$

where $x = \theta D_d / r_s$, $\kappa_s = \rho_s r_s / \Sigma_{cr}$ is the scale convergence, and the function $\mathcal{F}(x)$ is given by

$$\mathcal{F}(x) = \begin{cases} \sec^{-1}(x) / \sqrt{x^2 - 1} & (x > 1), \\ 1 & (x = 1), \\ \operatorname{sech}^{-1}(x) / \sqrt{1 - x^2} & (x < 1). \end{cases} \quad (12)$$

The deflection angle for the NFW profile can be derived as (Meneghetti et al. 2003)

$$\alpha(\theta) = \frac{2}{\theta} \int_0^\theta \theta' \kappa(\theta') d\theta' = \frac{4\kappa_s \theta_s}{x} [\ln(x/2) + \mathcal{F}(x)], \quad (13)$$

where $\theta_s = r_s / D_d$. The deflection potential for the NFW profile is then

$$\psi(\theta) = \int \alpha(\theta) d\theta = 2\kappa_s \theta_s^2 \left[\log^2\left(\frac{x}{2}\right) + (x^2 - 1)\mathcal{F}^2(x) \right]. \quad (14)$$

2.2.2 Jaffe profile

The Jaffe profile is given by

$$\rho(r) = \frac{\rho_s}{(r/r_s)^2 (1 + r/r_s)^2}, \quad (15)$$

where ρ_s and r_s are the scale density and radius, respectively. This profile reproduces well the $R^{1/4}$ surface brightness profile in projection with $r_s = R_{\text{eff}}/0.763$, where R_{eff} is the effective radius. The convergence for the Jaffe profile is given by (Jaffe 1983)

$$\kappa(\theta) = \kappa_s \left[\frac{\pi}{x} + 2 \frac{1 - (2 - x^2)\mathcal{F}(x)}{1 - x^2} \right], \quad (16)$$

where $x = \theta D_d / r_s$, $\kappa_s = \rho_s r_s / \Sigma_{cr}$ is the scale convergence, and $\mathcal{F}(x)$ is given in Equation (12). The deflection angle for the Jaffe profile can be derived as (Bartelmann & Meneghetti 2004)

$$\alpha(\theta) = 2\kappa_s \theta_s [\pi - 2x\mathcal{F}(x)], \quad (17)$$

where $\theta_s = r_s / D_d$. The deflection potential that reproduces the convergence in Equation (16) is

$$\psi(\theta) = 2\kappa_s \theta_s^2 [\pi x + \log(x^2) - 2(x^2 - 1)\mathcal{F}(x)]. \quad (18)$$

2.2.3 Power law mass profile

The elliptical power law model is often used to describe galaxy scale lenses (e.g. Suyu et al. 2013). In order to calibrate the uncertainty in our models we use the spherical power law mass density profile as a baseline comparison. This mass density profile is given by

$$\rho(r) = \rho_0 \left(\frac{r}{r_0} \right)^{-\gamma}. \quad (19)$$

The deflection angle for the power law mass profile is given by

$$\alpha(\theta) = \left(\frac{\theta_{\text{Ein}}}{\theta} \right)^{\gamma-2} \theta_{\text{Ein}}, \quad (20)$$

where θ_{Ein} is the Einstein radius.

3 CREATING MOCK DATA

In order to measure D_d and $D_{\Delta t}$, three sets of data are necessary: (1) imaging data of the lensed images of the quasar and its host galaxy, (2) time delays from a monitoring campaign, and (3) kinematics of the deflector. In this section we describe how we create mock data of each kind for a given strong lens system. First, in Section 3.1 we describe how we use a set of conjugate points to mimic the detailed modeling of the lensed quasar host, which would be otherwise too computationally expensive to carry out for large number of systems. Then, in Section 3.2 we describe how we create the full simulated datasets.

3.1 Mimicking extended source reconstruction with conjugate points

For the sake of speed, instead of carrying out a full extended source reconstruction analysis, we describe each extended source as a set of points, and analyze them with the so-called conjugate point techniques (Gavazzi et al. 2008). In order to obtain realistic results, we need to determine how many points to simulate and the associated astrometric uncertainty we want to associate with each one. The amount of information depends on both quantities, so we start by setting the latter and then adjust the former to obtain a realistic precision. Computing time depends on the number of points, so we adopt the smallest number that allows us to achieve realistic precision on the model parameters while keeping the computing time short enough for our purposes. In order to calibrate our model we focus on the slope of the mass density profile of a power law mass model, which is the main parameter controlling the velocity dispersion and time delay at fixed Einstein Radius (e.g. Wucknitz 2002; Suyu 2012). Thus, the minimum number of necessary source point is chosen such that, for a power-law deflector mass profile given in Equation (19), the power-law exponent can be inferred from the set of conjugate points with an uncertainty $\delta\gamma \sim 0.02$. We set this criterion to match with the precision on power-law slope γ attainable by current (Suyu et al. 2013; Wong et al. 2017) and future technologies (Meng et al. 2015) from a full-blown computationally intensive lens modeling effort.

We used a set of uniformly spaced points within a circle with 20 mas minimum separation between neighboring points to mimic an extended source. We assumed a power law mass profile given in Equation (19) for the deflector and created mock image data for the given source points. We set the uncertainty in the image position as $\sigma_\theta = 60$ mas (corresponding to approximately half a pixel on the HST Wide Field Camera 3 infrared channel). The mock lens system in our analysis only produces two lensed images due to the assumed spherical symmetry. In doubly-imaged lens systems, there is a degeneracy between the power-law slope γ and the Einstein radius θ_{Ein} for asymmetric lens configurations whereas θ_{Ein} is completely independent of γ for a perfectly symmetric lens configuration (Suyu 2012). Therefore, the number of conjugate points with fixed positional uncertainty needed to achieve a particular $\delta\gamma$ by breaking this degeneracy depends on the asymmetry of the lens configuration. We fix $\beta_{\text{centre}} = \theta_{\text{Ein}}/2$ for the rest of this study

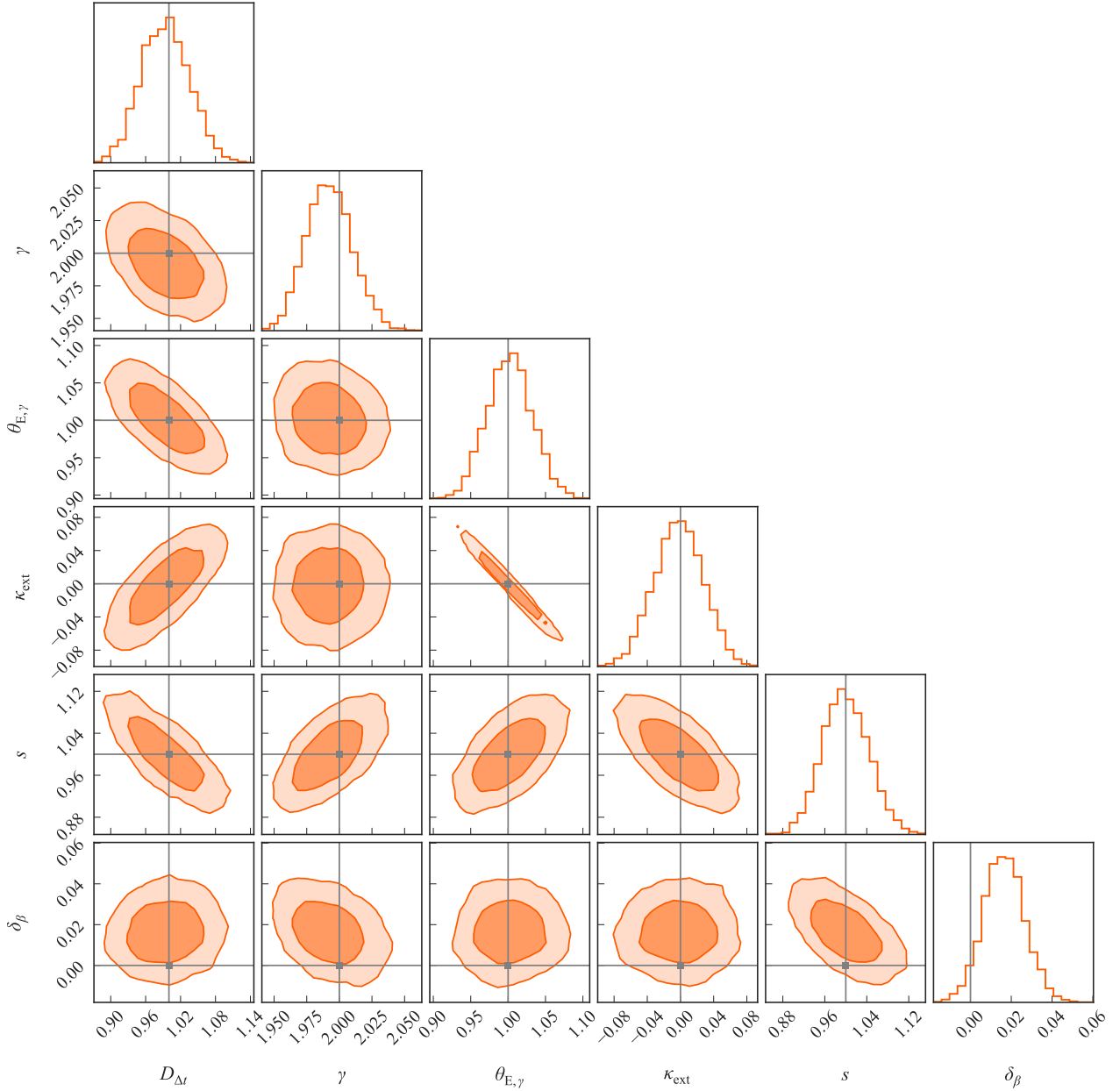


Figure 1. Posterior PDF of the model parameters for a power-law mass profile inferred from lensing data with 230 conjugate points. $D_{\Delta t}$, $\theta_{E,\gamma}$, and δ_β are normalized with $D_{\Delta t}^{\text{fiducial}}$, θ_E , and θ_E , respectively, where θ_E is the true Einstein radius of the lens system. Grey lines show the true values of the parameters and orange contours show the 1σ and 2σ confidence regions. The uncertainty on the power law slope is $\delta\gamma = 0.02$ and the time-delay distance $D_{\Delta t}$ is simultaneously estimated with 4.2% uncertainty for an assumed Gaussian prior with 3% uncertainty on $(1 - \kappa_{\text{ext}})$.

which is the case in the middle between the two extremes of perfect symmetry and maximal asymmetry.

We tuned this setup to give realistic errors on model parameters by analyzing mock data to obtain the posterior probability distribution function (PDF) of the model parameters: the power law slope of the mass profile γ , the Einstein radius θ_{Ein} , and the source-point positions β . From Bayes' theorem, the posterior PDF follows

$$P(\gamma, \theta_{\text{Ein},\gamma}, \beta, \kappa_{\text{ext}} | \theta) \propto P(\theta | \gamma, \theta_{\text{Ein},\gamma}, \beta, \kappa_{\text{ext}}) P(\gamma, \theta_{\text{Ein},\gamma}, \beta, \kappa_{\text{ext}}), \quad (21)$$

where θ is the mock data for image positions, $\theta_{\text{Ein},\gamma}$ is the

Einstein radius for the power-law mass profile, and κ_{ext} is the external convergence. The first term on the right-hand side is the likelihood of the data given the model parameters, and the second one is the prior PDF of the model parameters.

To sample from the posterior PDF through the Markov Chain Monte Carlo (MCMC) method, we use the *cosmoHammer* package (Akeret et al. 2013), which embeds *emcee* (Foreman-Mackey et al. 2013), a Python implementation of an affine-invariant ensemble sampler for MCMC proposed by Goodman & Weare (2010). We first find the maxima of the likelihood function for the given image positions treating the source-point positions uncorrelated using the particle swarm

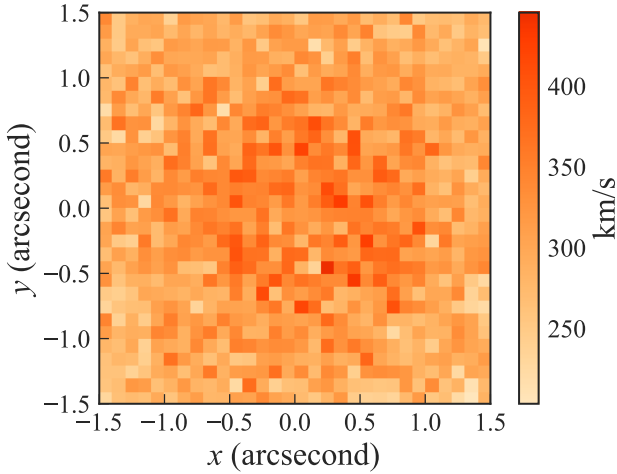


Figure 2. Line-of-sight velocity dispersion for a combination of NFW (dark component) and Jaffe (luminous component) profiles. 5% random Gaussian noise was added to the velocity dispersion and it was smoothed with a Gaussian of FWHM=0.1'' to take the effect of seeing into account.

Table 1. Priors for joint analysis with power-law mass profile

Parameter	Prior
$D_{\Delta t}$	uniform in $[0, 2] \times D_{\Delta t}^{\text{fiducial}}$ *
γ	uniform in $[1, 3]$
$\theta_{\text{Ein}, \gamma}$	uniform in $[0.5, 2]''$
κ_{ext}	Gaussian with 3% uncertainty on $(1 - \kappa_{\text{ext}})$
s	uniform in $[0, 2]$
$\delta\beta$	uniform in $[-0.5, 0.5]''$

* $D_{\Delta t}^{\text{fiducial}}$ is the fiducial value of the time-delay distance.

optimization routine (Kennedy & Eberhart 1995) included in *cosmoHammer*. We tuned the settings of the optimization process to find the maxima with $\sim 99\%$ accuracy. We then treat the source-point positions at the maxima of the likelihood function as the reconstructed source. We sample from the posterior PDF of the source-point positions as

$$\beta_{\text{sampled}} = s\beta_{\text{reconstructed}} + \delta\beta, \quad (22)$$

using two parameters: a rescaling factor s for the source plane, and an offset $\delta\beta$. Equation (22) is essentially a SPT (Schneider & Sluse 2014)

$$\beta \rightarrow \beta' = [1 + f(\beta)]\beta, \quad (23)$$

which is a generalization of the MST and leaves the strong lensing properties invariant. This allows us to incorporate the degeneracies induced by the SPT into our model.

We impose a Gaussian prior with 3% uncertainty for $(1 - \kappa_{\text{ext}})$ and uniform priors in appropriately large ranges for all the other parameters. The details of the chosen priors are given in Table 1. After performing this analysis for various numbers of source points, we find that the uncertainty of the power law exponent achieves our target $\delta\gamma \sim 0.02$ for a source with 230 points (Figure 1). In comparison, a conservative choice of $\delta\gamma \sim 0.04$ can be achieved by adopting a source with 130 points. We also jointly sample the posterior PDF

of the time-delay distance $D_{\Delta t}$ by adding a mock time-delay measurement to the dataset. The posterior PDF of the joint analysis is

$$P(\xi|\theta, \Delta t) \propto P(\theta, \Delta t|\xi)P(\xi) \propto P(\theta|\xi)P(\Delta t|\xi)P(\xi), \quad (24)$$

where ξ are the model parameters $\{D_{\Delta t}, \gamma, \theta_{\text{Ein}, \gamma}, \kappa_{\text{ext}}, s, \delta\beta\}$. The second line in Equation (24) is implied because the image positions and the time-delay data are independent measurements. The marginalized uncertainty of $D_{\Delta t}$ from the joint analysis is 4.2% which is comparable to the state of the art measurements of the time-delay distance (Suyu et al. 2013; Wong et al. 2017) after taking the difference in the uncertainty of κ_{ext} into account. We thus conclude that the analysis of 230 correlated points with positional uncertainty 60 mas with a spherical model approximates well the extended source reconstruction with a non-spherical model as far as the main parameters controlling D_d and $D_{\Delta t}$ are concerned. Therefore, we adopt this setup when we analyze two component mass models.

3.2 Mock lensing data with spatially resolved velocity dispersion

We choose a composite mass model for the deflector galaxy assuming the NFW profile for the dark matter component and the Jaffe profile for the luminous matter component.

We assumed that in projection one-third of the total mass comes from the dark matter component within half of the half-light radius (Auger et al. 2010), to obtain the normalizations for the NFW and Jaffe profiles.

First, we created mock lensing data for 230 conjugate points for the adopted deflector mass profile. Random Gaussian noise with standard deviation $\sigma_\theta = 60$ mas was added to the conjugate point positions.

The velocity dispersion profile for a mass distribution can be obtained by solving the spherical Jean's equation, which is given by

$$\frac{1}{l(r)} \frac{d(l\sigma_r^2)}{dr} + 2\beta_{\text{ani}}(r) \frac{\sigma_r^2}{r} = -\frac{GM(\leq r)}{r^2}. \quad (25)$$

Here, $l(r)$ is the luminosity density of the galaxy, σ_r is the radial velocity dispersion, and $\beta_{\text{ani}}(r)$ is the anisotropy profile given by

$$\beta_{\text{ani}} = 1 - \frac{\sigma_t^2}{\sigma_r^2}, \quad (26)$$

where σ_t is the tangential velocity dispersion for a spherically symmetric mass distribution. The surface-brightness-weighted, line-of-sight velocity dispersion can be obtained by solving this equation as (Mamon & Lokas 2005)

$$I(R)\sigma_{\text{los}}^2(R) = 2G \int_R^\infty k\left(\frac{r}{R}, \frac{r_{\text{ani}}}{R}\right) l(r) M(r) \frac{dr}{r}, \quad (27)$$

where $I(R)$ is the surface brightness. For Osipkov-Merritt anisotropy parameter $\beta_{\text{ani}}(r) = 1/(1 + r_{\text{ani}}^2/r^2)$ (Osipkov 1979; Merritt 1985a,b), the function $k(u, u_{\text{ani}})$ is given by

$$k(u, u_{\text{ani}}) = \frac{u_{\text{ani}}^2 + 1/2}{(u_{\text{ani}}^2 + 1)^{3/2}} \left(\frac{u^2 + u_{\text{ani}}^2}{u} \right) \tan^{-1} \sqrt{\frac{u^2 - 1}{u_{\text{ani}}^2 + 1}} - \frac{1/2}{u_{\text{ani}}^2 + 1} \sqrt{1 - 1/u^2}. \quad (28)$$

Using Equation (27), we computed the line-of-sight velocity dispersion weighted by surface brightness in a given bin size (e.g. $0.1''$). To take seeing into account, we convolved the surface-brightness-weighted line-of-sight velocity dispersion image with a Gaussian kernel of a given full width at half maximum (FWHM) and then normalized it to obtain the line-of-sight velocity dispersion as

$$\tilde{\sigma}_{\text{los}}^2(x, y) = \frac{I \sigma_{\text{los}}^2 * g(x, y)}{I * g(x, y)}, \quad (29)$$

where $g(x, y)$ is a 2-dimensional Gaussian function, and the symbol $*$ denotes the convolution (Figure 2). Finally, we added random Gaussian noise with a given standard deviation to each pixel. We also added a random Gaussian noise with 2% standard deviation to the time delay, typical of the best measurements (e.g. Bonvin et al. 2017).

4 PRECISION ON COSMOLOGICAL DISTANCE MEASUREMENTS

In this section we use the mock data created as described in the previous section to estimate the uncertainties of the angular diameter and time-delay distances using the MCMC method.

We performed a joint analysis to obtain the posterior PDF of the model parameters ξ given the mock lensing data with velocity dispersion and the time delay data. From Bayes' theorem, the posterior PDF follows

$$P(\xi | \theta, \sigma_*, \Delta t) \propto P(\theta, \sigma_*, \Delta t | \xi) P(\xi), \quad (30)$$

where $P(\theta, \sigma_*, \Delta t | \xi)$ is the likelihood of the data given the model parameters, $P(\xi)$ is the prior PDF of the model parameters, θ is the image position data, σ_* is the velocity dispersion data, Δt is the time delay between images, and ξ contains all the model parameters $\{D_d, D_{\Delta t}, \kappa_s^{\text{NFW}}, r_s^{\text{NFW}}, \kappa_s^{\text{Jaffe}}, r_s^{\text{Jaffe}}, r_{\text{ani}}, \kappa_{\text{ext}}, \beta\}$. As the image positions, the velocity dispersion, and the time delay are independent data, the likelihood of the data given the model parameters can be written as

$$P(\theta, \sigma_*, \Delta t | \xi) = P(\theta | \xi) P(\sigma_* | \xi) P(\Delta t | \xi). \quad (31)$$

As it is often the case in high dimensional spaces, it is important to choose the priors carefully (e.g. Brewer et al. 2014). If the priors are not carefully chosen, the marginalized 1-dimensional posteriors on each parameter can be significantly skewed (e.g. Birrer et al. 2016), resulting in the median and mode of the PDF to be a biased estimator of the true value. Naturally this bias can be mitigated or eliminated by using the full PDF and not just point estimators. However, it is important to use priors that are as informative as possible. We impose Gaussian priors on r_s^{Jaffe} and κ_{ext} , as r_s^{Jaffe} can be measured directly by fitting the surface brightness profile of the lens, whereas κ_{ext} can be inferred indirectly by comparing the statistics of galaxies along the line of sight to the lens with simulated light cones (Hilbert et al. 2009; Suyu et al. 2013; Greene et al. 2013; Collett et al. 2013; Rusu et al. 2017). We set a Gaussian prior for r_s^{NFW} with 20% uncertainty. Note, this is a conservative choice compared to the 14% uncertainty adopted by Wong et al. (2017) based on the results of Gavazzi et al. (2007). We choose Jeffrey's prior $P(\xi) \propto 1/\xi$ for κ_s^{NFW} and κ_s^{Jaffe} . We tested two

Table 2. Priors for joint analysis with composite mass model

Parameter	Prior
D_d	uniform in $[0, 2] \times D_d^{\text{fiducial}}$ *
$D_{\Delta t}$	uniform in $[0, 2] \times D_{\Delta t}^{\text{fiducial}}$ *
κ_s^{NFW}	Jeffrey's prior
r_s^{NFW}	Gaussian with 20% uncertainty
κ_s^{Jaffe}	Jeffrey's prior
r_s^{Jaffe}	Gaussian with 2% uncertainty
r_{ani}	uniform prior for β_{ani} in $[0, 1]$
κ_{ext}	Gaussian prior on $(1 - \kappa_{\text{ext}})$
s	uniform in $[0, 2]$
$\delta\beta$	uniform in $[-0.5, 0.5]''$

* D_d^{fiducial} and $D_{\Delta t}^{\text{fiducial}}$ are the fiducial values of the angular diameter distance to the deflector and the time-delay distance.

prior choices for r_{ani} : (a) uniform in $[0.5, 5] \times R_{\text{eff}}$ (hereafter referred as $P_{[0.5, 5]}(r_{\text{ani}}/R_{\text{eff}})$, as used in Suyu et al. 2012; Birrer et al. 2016; Wong et al. 2017), and (b) a uniform prior for $\beta_{\text{ani}}(R_{\text{eff}})$ in $[0, 1]$ (hereafter referred as $P_{[0, 1]}(\beta_{\text{ani}}(R_{\text{eff}}))$). $P_{[0, 1]}(\beta_{\text{ani}}(R_{\text{eff}}))$ puts more weight in the region $r_{\text{ani}}/R_{\text{eff}} < 2$, where the assumed value of r_{ani} in our model lies, in comparison with $P_{[0.5, 5]}(r_{\text{ani}}/R_{\text{eff}})$ and it results in a more unbiased and constrained estimate of the angular diameter distance D_d (Figure 3). Adopting a more restricting uniform prior for r_{ani} in $[0.5, 2] \times R_{\text{eff}}$ produces a similar constraint on D_d as the one by adopting $P_{[0, 1]}(\beta_{\text{ani}}(R_{\text{eff}}))$. We set $P_{[0, 1]}(\beta_{\text{ani}}(R_{\text{eff}}))$ as the prior for r_{ani} for the rest of this study.

We have examined the effect of having spatially resolved velocity dispersion data on the uncertainties of the model parameters by studying three cases: (1) without any kinematics, (2) with integrated velocity dispersion data of the deflector within $1.2''$ radius, and (3) with spatially resolved velocity dispersion data. We adopted three observational settings, which reflect variation in qualities of observation instruments and conditions. These settings are (1) “baseline”: representative of the resolution and precision that can be achieved with integral field spectrographs (IFSs) on current and upcoming instruments, e.g. OSIRIS on Keck or NIRSPEC on the JWST, with the precision on the velocity dispersion and the external convergence that can be expected in the best cases, (2) “conservative”: same as baseline but with conservative precision on the velocity dispersion and the external convergence, and (3) “futuristic”: for IFSs on upcoming extremely large telescopes, e.g. IRIS on Thirty Meter Telescope (TMT) (Table 3). It is beyond the scope of this paper to estimate the amount of exposure time required to meet these goals for each one of the instrumental setups and to analyze the sources of systematic uncertainties. This exploration is left for future work.

As expected, D_d can only be measured by adding the stellar kinematic information to the lensing and time-delay data (Figure 4). When integrated stellar kinematics is added, the anisotropy radius r_{ani} is not constrained due to the mass-anisotropy degeneracy. Given our parametrization and assumptions, D_d absorbs most of the improvement after adding the integrated stellar kinematics, since the precision of $D_{\Delta t}$ is limited by the assumed priors on time delay and external convergence. If one were to consider more flexible models, the gain would be even more significant, highlight-

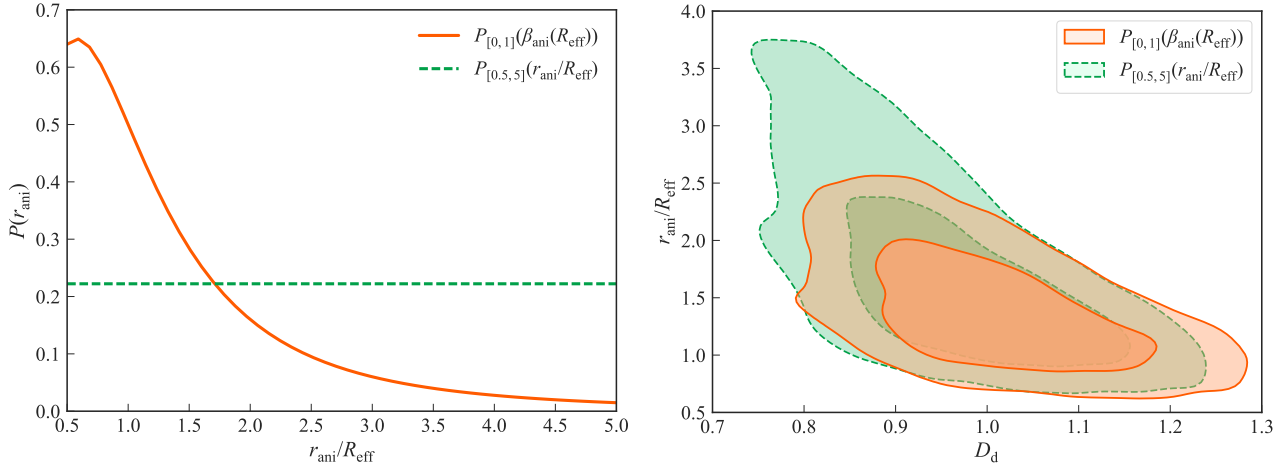


Figure 3. Priors for the anisotropy radius r_{ani} (left) and their effects on the mass-anisotropy degeneracy breaking (right). The two chosen priors are uniform prior for r_{ani} in $[0.5, 5] \times R_{\text{eff}}$ (labelled $P_{[0.5,5]}(r_{\text{ani}}/R_{\text{eff}})$, solid) and uniform prior for $\beta_{\text{ani}}(R_{\text{eff}})$ in $[0, 1]$ (labelled $P_{[0,1]}(\beta_{\text{ani}}(R_{\text{eff}}))$, dashed). In the right plot, the contours represent 1σ and 2σ confidence regions and D_d is normalized with D_d^{fiducial} . $P_{[0,1]}(\beta_{\text{ani}}(R_{\text{eff}}))$ puts more weight in the region $r_{\text{ani}}/R_{\text{eff}} < 2$, where the assumed value of r_{ani} in our model lies, in comparison with $P_{[0.5,5]}(r_{\text{ani}}/R_{\text{eff}})$ and it leads to a more unbiased and constrained estimate of the angular diameter distance D_d .

ing the importance of kinematics. In the real world of course, having additional information is not only helpful for improving the precision but also for checking for systematics and improving the accuracy. Using spatially resolved velocity dispersion data can improve uncertainty on D_d from $\sim 20\%$ to $\sim 10\%$ for the baseline setup and from $\sim 27\%$ to $\sim 17\%$ for the conservative setup with respect to using integrated velocity dispersion data. Moreover, the anisotropy radius r_{ani} is well-determined only when spatially resolved kinematics is introduced (Figure 4), which demonstrates that spatially resolved kinematics help break the mass-anisotropy degeneracy and allow us to use the anisotropy radius r_{ani} as a free parameter. For our adopted lensing data quality equivalent to $\delta\gamma \sim 0.02$, the lens model parameters are limited by modeling uncertainties, thus the addition of the spatially resolved kinematics improves the constraints only by $\sim 1\%$. If we adopt a conservative lensing data quality equivalent to $\delta\gamma \sim 0.04$, the addition of the spatially resolved kinematics leads to more relative improvement in the constraints on the model parameters, e.g. uncertainty on $D_{\Delta t}$ improves by $\sim 3\%$ compared to the case with only integrated kinematics. In comparison to our adopted lensing data quality ($\delta\gamma \sim 0.02$), this conservative lensing data quality worsens the constraint $D_{\Delta t}$ by $\sim 2\%$ (from $\sim 6\%$ to $\sim 8\%$). The constraint on D_d does not significantly change (within 1%), as D_d is limited by the quality of the stellar kinematics data. The uncertainties on D_d and $D_{\Delta t}$ for different datasets and observational setups are summarized in Table 4. To check for bias in point estimators of the model parameters, we performed 25 joint analyses for different noise realizations using the same lensing parameters with the “baseline” setup. The 1σ regions of the parameter estimates from these analyses are shown in with horizontal error bars in the 1-dimensional histograms of Figure 4. All the point estimators of the model parameters are within 1σ of the true values. We note however, that it is highly preferable to not adopt point estimators of individual parameters, but rather take into account the full (asymmetric) posterior probability distribution function.

5 COSMOLOGICAL INFERENCE

Having estimated the precision attainable on the two distances for a single lens, we now turn to the estimation of cosmological parameters from samples of time delay lenses. First, in Section 5.1. we investigate the precisions achievable from time delay lensing data alone. Then, in Section 5.2, we combine the lensing information with *Planck* data to illustrate complementarity in the determination of the cosmological parameters.

5.1 Cosmology from strong lensing alone

We performed a Bayesian analysis to obtain the posterior PDF of the cosmological parameters \mathbf{C} given the inferred angular diameter and time-delay distances computed in Section 4. The posterior PDF is given by Bayes’ theorem as

$$P(\mathbf{C}|\mathbf{D}, \mathbf{z}) \propto P(\mathbf{D}|\mathbf{C}, \mathbf{z})P(\mathbf{C}), \quad (32)$$

where \mathbf{D} is the set of measurements of D_d and $D_{\Delta t}$ for the strong lenses, and \mathbf{z} is the set of redshifts pairs (z_d, z_s) for the lenses. To efficiently compute the likelihood term $P(\mathbf{D}|\mathbf{C}, \mathbf{z})$, we approximate the posterior PDF of D_d and $D_{\Delta t}$ of each lens by its best fit bivariate normal distribution function as

$$P(D_d, D_{\Delta t}) = \frac{1}{2\pi\sigma_{D_d}\sigma_{D_{\Delta t}}\sqrt{1-\rho_{\text{cor}}^2}} \exp\left[-\frac{z(D_d, D_{\Delta t})}{2(1-\rho_{\text{cor}}^2)}\right], \quad (33)$$

where

$$z(D_d, D_{\Delta t}) = \frac{(D_d - \mu_{D_d})^2}{\sigma_{D_d}^2} + \frac{(D_{\Delta t} - \mu_{D_{\Delta t}})^2}{\sigma_{D_{\Delta t}}^2} - \frac{2\rho_{\text{cor}}(D_d - \mu_{D_d})(D_{\Delta t} - \mu_{D_{\Delta t}})}{\sigma_{D_d}\sigma_{D_{\Delta t}}}, \quad (34)$$

and $\rho_{\text{cor}} = \text{cov}(D_d, D_{\Delta t})/\sigma_{D_d}\sigma_{D_{\Delta t}}$ with $\text{cov}(D_d, D_{\Delta t})$ being the covariance between the two distances. μ_{D_d} and $\mu_{D_{\Delta t}}$ are the means of D_d and $D_{\Delta t}$, respectively. Assuming the posterior PDF as a bivariate normal distribution function is accurate

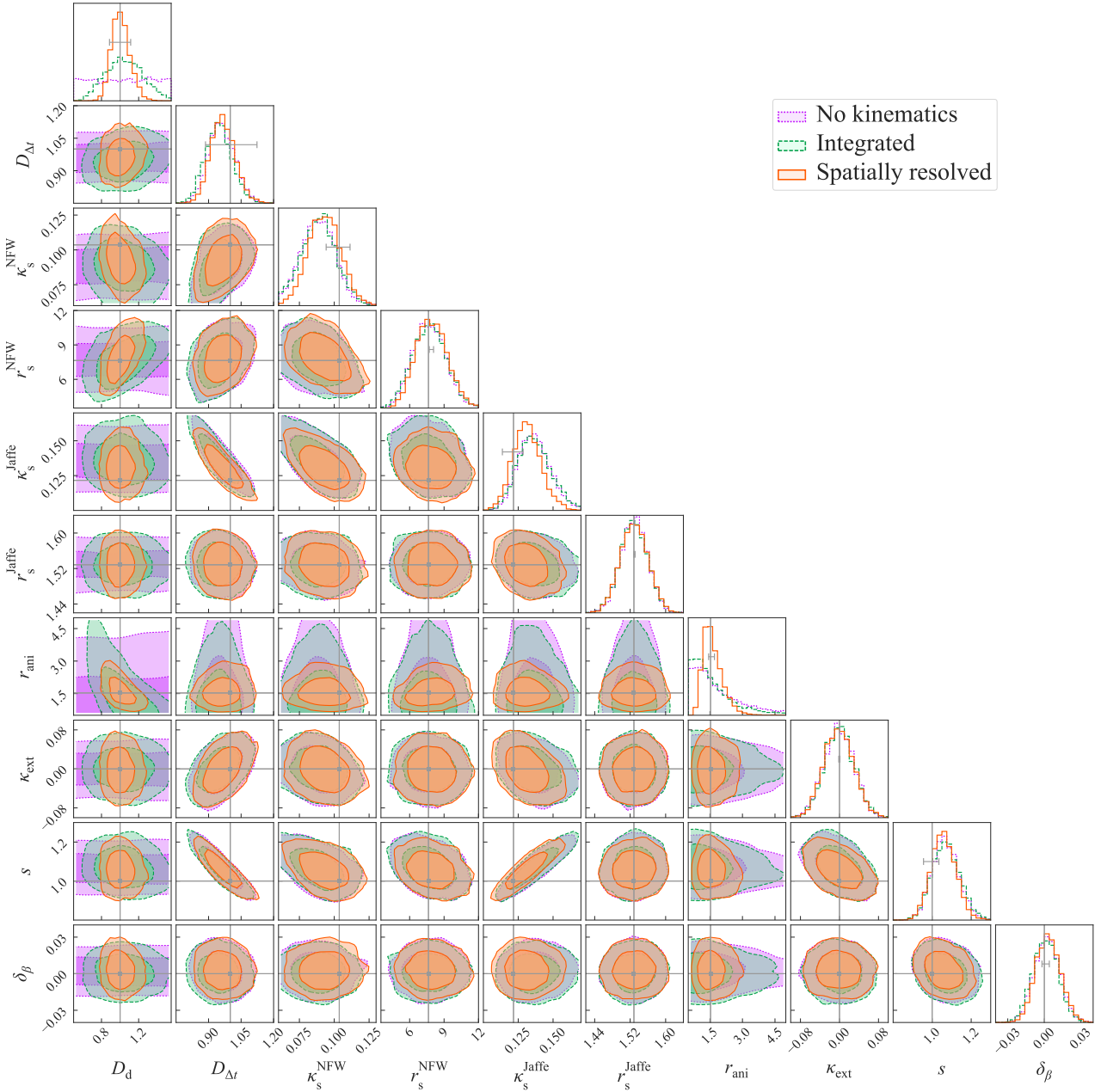


Figure 4. Posterior PDF of the model parameters given from joint analysis with lensing and time delay data with spatially resolved kinematics (solid), with integrated kinematics (dashed), and without any kinematics (dotted). The contours for each case represent 1σ and 2σ confidence regions. The model parameters D_d , $D_{\Delta t}$, r_s^{NFW} , r_s^{Jaffe} , r_{ani} , and δ_β are normalized with D_d^{fiducial} , $D_{\Delta t}^{\text{fiducial}}$, R_{Ein} , R_{Ein} , R_{Ein} , and θ_{Ein} , respectively, where R_{Ein} is the true Einstein radius with the dimension of length. Grey solid lines show the true values of the parameters. D_d can only be determined with kinematics. The anisotropy radius r_{ani} is also well determined with kinematics showing that the mass-anisotropy degeneracy is overcome.

to the order of Fisher matrix approximation. As we are only interested in the precision of cosmological parameters, we choose μ_{D_d} and $\mu_{D_{\Delta t}}$ to be the fiducial values of the angular and time-delay distances.

The quoted uncertainties on the parameters are determined from the 16- and 84-percentiles of the posterior PDF. We have considered six different cosmological models for this analysis (Table 6). The first one is the basic flat Λ CDM model. The next three models are one-parameter extensions of the basic Λ CDM model for Ω_K , w , and N_{eff} , labelled as

$\text{o}\Lambda\text{CDM}$, $w\text{CDM}$, and $N_{\text{eff}}\text{CDM}$ models, respectively. The last two cosmological models are two-parameter extensions from the basic Λ CDM model, relaxing (Ω_K, w) and (w_0, w_a) , labelled as owCDM and $w_a\text{CDM}$ models, respectively. In the $w_a\text{CDM}$ model, the dark-energy equation-of-state parameter w is given by

$$w(a) = w_0 + w_a(1 - a), \quad (35)$$

where, a is the scale factor. We examined the parameter

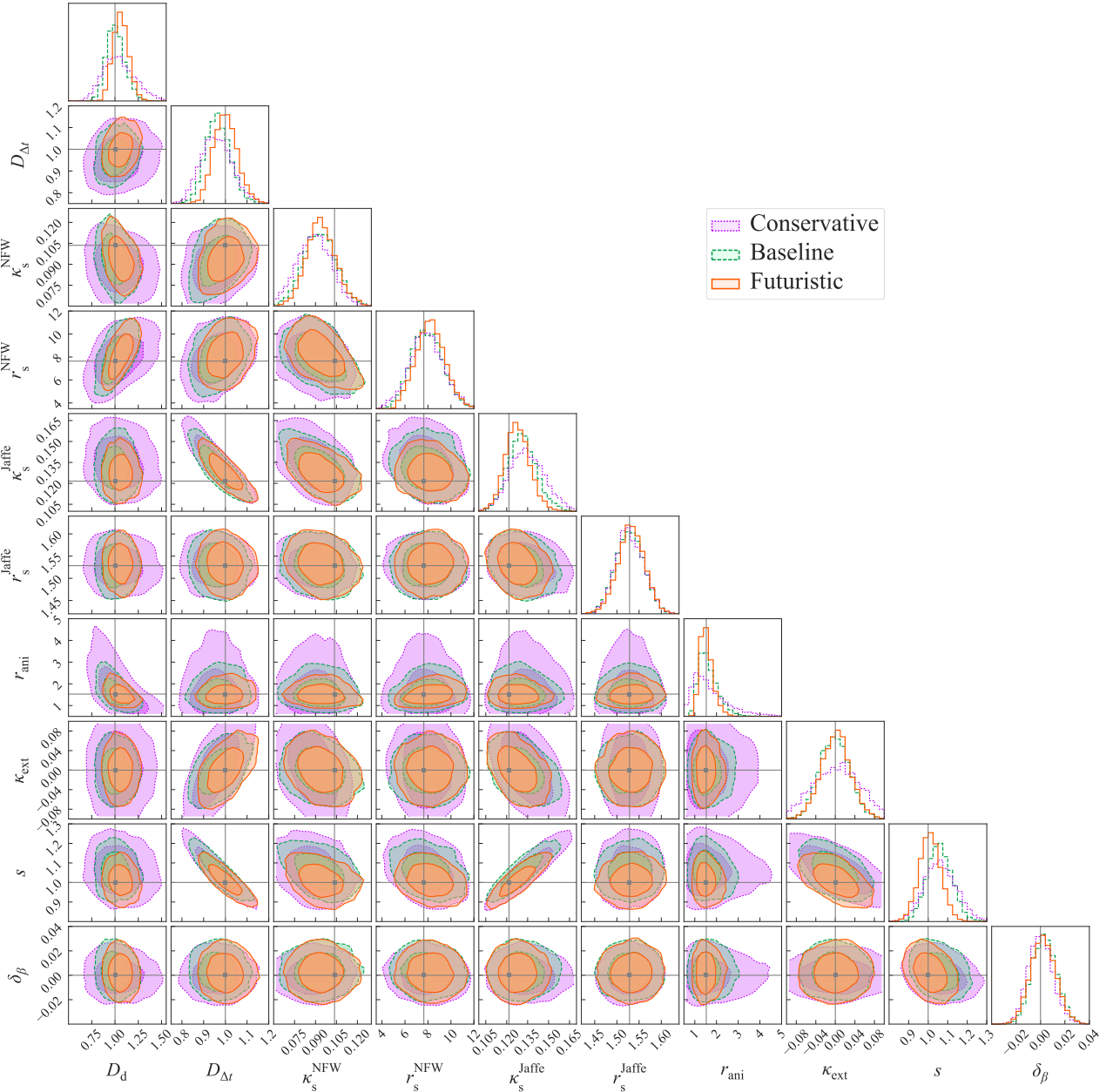


Figure 5. Posterior PDF of the model parameters given from joint analysis with lensing and time delay data with spatially resolved kinematics for baseline (dashed), futuristic (solid), and conservative (dotted) setups. The contours for each case represent 1σ and 2σ confidence regions. The model parameters D_d , $D_{\Delta t}$, r_s^{NFW} , r_s^{Jaffe} , r_{ani} , and δ_β are normalized with $D_d^{fiducial}$, $D_{\Delta t}^{fiducial}$, R_{Ein} , R_{Ein} , R_{Ein} , and θ_{Ein} , respectively, where R_{Ein} is the true Einstein radius with the dimension of length. Grey solid straight lines show the true values of the parameters. The constraints on the model parameters become tighter with higher quality of spatially resolved stellar kinematics.

uncertainties primarily using the fiducial cosmology: $H_0 = 70$ km/s/Mpc, $\Omega_m = 0.3$, $\Omega_\Lambda = 0.7$, $\Omega_K = 0$, $w = -1$.

First, we explored the uncertainties on the cosmological parameters achievable by using nine real lenses for which accurate time delay measurements and deep HST imaging data are readily available. The details of these nine lenses are given in Table 5. Out of these nine lenses, we consider six lenses to have spatially resolved kinematics and the remaining three to have integrated kinematics from the “baseline” observational setup, since three of the lenses are currently outside of the reach of OSIRIS on Keck. Spatially

resolved kinematics for all nine systems could be obtained with JWST, so our estimate should be considered as conservative in this respect. Then, to explore the strength of using strong lenses to measure the cosmological parameters, we repeated the analysis for a simulated sample of 40 strong lenses expected to be available in the next few years through dedicated follow-up of newly discovered systems. Thus, we created a mock catalog of 31 lenses with a redshift distribution that resembles the one for the nine lenses given in Table 5 in the following manner. First, we fit a Gaussian distribution to the redshift distribution of deflectors of the

Table 3. Parameters for different observational setups

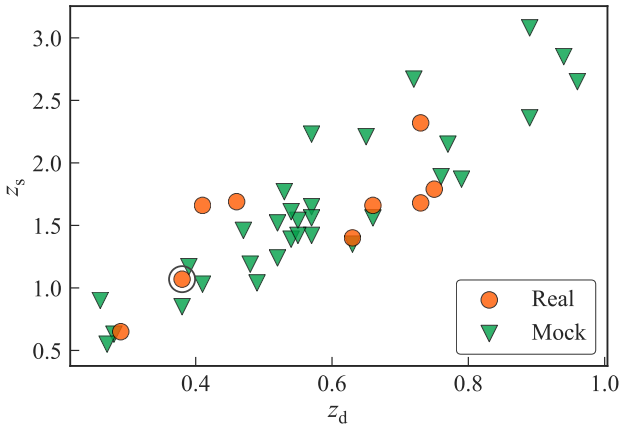
Observational setup*	Annulus width (arcsecond)	$N_{\text{annuli}}^\dagger$	PSF FWHM (arcsecond)	Parameter Uncertainties				
				a_{Jaffe} (%)	$1 - \kappa_{\text{ext}}$ (%)	Δt (%)	σ_s (%)	θ (mas)
Baseline	0.1	12	0.1	2	3	2	5	60
Conservative	0.2	6	0.1	2	5	2	10	60
Futuristic	0.05	24	0.03	2	3	2	5	60

* The “baseline” and “conservative” setups represent what we can expect to obtain with current and upcoming diffraction limited integral field spectrographs, e.g. OSIRIS on Keck and NIRSPEC on JWST. The “futuristic” setup is for diffraction limited integral field spectrographs on upcoming extremely large telescopes, e.g. TMT or E-ELT.

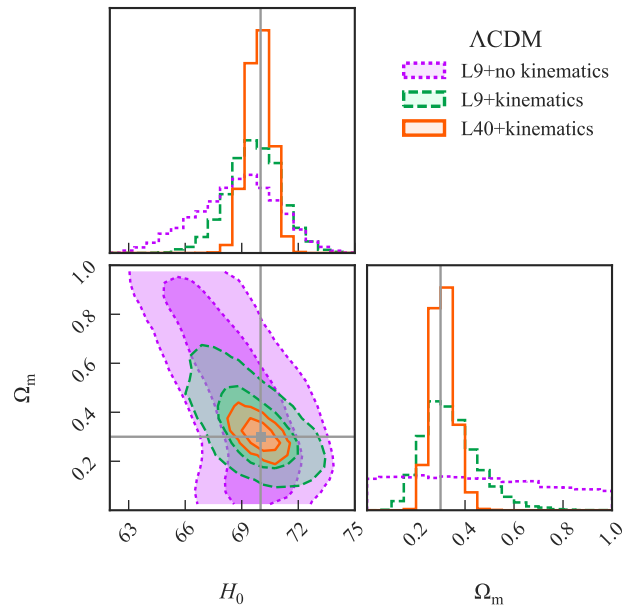
$^\dagger N_{\text{annuli}}$ refers to the number of annuli for the spatially resolved kinematics for each observational setup.

Table 4. Uncertainties of D_d and $D_{\Delta t}$ for a single lens with different observational setups

Model	Kinematics data	σ_{D_d} (%)	$\sigma_{D_{\Delta t}}$ (%)
Baseline	No	-	6.5
	Integrated	19.8	6.5
	Resolved	9.6	5.8
Conservative	Integrated	27.0	7.8
	Resolved	16.7	7.5
Futuristic	Resolved	7.7	5.3

**Figure 6.** Distribution of deflector and source redshifts of the lenses. The circles show the redshifts for the nine actual lenses with measured time delays and deep HST imaging. The triangles show the redshifts for the 31 lenses in the mock catalog. We assume a fiducial redshift $z_d = 0.38$ for the strong lens HS2209 as it has not been accurately measured yet and it is marked with a dark circle on the plot.

nine lenses and sampled from this fitted Gaussian distribution. Next, we also fit a Gaussian distribution to the distribution of the ratios of the deflector and source redshifts from the nine lenses and sampled from this distribution to determine the source redshift for each of the 31 mock lensing systems. The redshift distribution of the real and mock lenses is shown in Figure 6.

**Figure 7.** Posterior PDF of cosmological parameters for the flat Λ CDM model obtained from distance measurements for nine lenses (L9) without kinematics (dotted), for nine lenses with kinematics (dashed) and for 40 lenses (L40) with kinematics (solid). The contours represent 1σ and 2σ confidence regions. Solid straight lines show the fiducial values. Using kinematics breaks the degeneracy between parameters and improves the precision on H_0 from 3.2% to 2.0% for nine lenses.

5.1.1 Nine lenses

The detailed parameter uncertainties for all the cosmological model considered in this paper are tabulated in Table 7. For the flat Λ CDM model, H_0 is estimated with 2.0% precision (69.7 ± 1.4 km/s/Mpc) and Ω_m is estimated with precision $\sigma(\Omega_m) = 0.11$.

To measure the improvement over cosmological parameter uncertainties by using spatially resolved kinematics, we did the same analysis for nine lenses without using kinematics. In that case, the parameter uncertainties are $\sigma(H_0) = 3.2\%$ and $\sigma(\Omega_m) = 0.32$. Using spatially resolved kinematics for nine lenses leads to an improvement in the precision of H_0 from 3.2% to 2.0%. If we adopt the conservative lensing data quality equivalent to $\delta\gamma \sim 0.04$, addition

Table 5. Uncertainties of D_d and $D_{\Delta t}$ for different lens systems

Lens system	z_d	z_s	Velocity dispersion data	σ_{D_d} (%)	$\sigma_{D_{\Delta t}}$ (%)
HE0047	0.41	1.66	Resolved	9.6	5.9
J1206	0.75	1.79	Resolved	8.8	5.4
HE0435	0.46	1.69	Resolved	9.5	7.0
HE1104	0.73	2.32	Resolved	9.1	5.5
RXJ1131	0.29	0.65	Resolved	10.0	6.6
J0246	0.73	1.68	Resolved	8.9	5.5
HS2209	0.38*	1.07	Integrated	21.7	7.0
WFI2033	0.66	1.66	Integrated	18.5	6.1
B1608	0.63	1.39	Integrated	19.8	6.1

* The deflector redshift for HS2209 has not been accurately measured yet, therefore we used a fiducial redshift of $z = 0.38$. The results are not sensitive to the assumed redshift.

Table 6. Cosmological models and parameter priors

Model name	Description	Priors
Λ CDM	Flat Λ CDM cosmology	$h \in [0, 1.5], \Omega_m \in [0, 1]$
o Λ CDM	Non-flat Λ CDM cosmology	$h \in [0, 1.5], \Omega_\Lambda \in [0, 1], \Omega_k \in [-0.5, 0.5], \Omega_m > 0$
wCDM	Flat wCDM cosmology	$h \in [0, 1.5], \Omega_\Lambda \in [0, 1], w \in [-2.5, 0.5]$
N_{eff} CDM	Flat N_{eff} CDM cosmology	$h \in [0, 1.5], \Omega_\Lambda \in [0, 1], N_{\text{eff}} \in [1, 5]$
owCDM	Non-flat wCDM cosmology	$h \in [0, 1.5], \Omega_\Lambda \in [0, 1], \Omega_k \in [-0.5, 0.5], \Omega_m > 0, w \in [-2.5, 0.5]$
w_a CDM	Flat w_a CDM cosmology	$h \in [0, 1.5], \Omega_\Lambda \in [0, 1], w_0 \in [-2.5, 0.5], w_a \in [-8, 4.5]$

of the spatially resolved stellar kinematics for nine lenses still improves the precision of H_0 by 1% from 3.9% to 2.9%. Without any kinematics there is a very strong degeneracy in Ω_m , which can be broken by adding the stellar kinematics information (Figure 7).

For the o Λ CDM model with our “primary” fiducial cosmology, the cosmological parameter uncertainties are estimated to be $\sigma(H_0) = 3.3\%$, $\sigma(\Omega_m) = 0.2$, $\sigma(\Omega_K) = 0.27$ (Figure 8). For the flat wCDM model, we estimate the cosmological parameters uncertainties to be $\sigma(H_0) = 6.2\%$, $\sigma(\Omega_m) = 0.13$, and $\sigma(w) = 0.57$ (Figure 8). For the N_{eff} CDM model, the parameter uncertainties are estimated to be $\sigma(H_0) = 2.0\%$, $\sigma(\Omega_m) = 0.11$ and N_{eff} is completely degenerate.

For the owCDM model, where we relax Ω_K and w from the flat Λ CDM model, we estimate the parameters with uncertainties $\sigma(H_0) = 6.5\%$, $\sigma(\Omega_m) = 0.22$, $\sigma(\Omega_K) = 0.28$, $\sigma(w) = 0.63$. For the w_a CDM model, w_0 and w_a are estimated with uncertainties $\sigma(w_0) = 0.82$ and $\sigma(w_a) = 3.5$, respectively.

5.1.2 40 lenses

For the flat Λ CDM model, using distance measurement uncertainties from 40 lenses we estimate H_0 with 0.92% precision and Ω_m with $\sigma(\Omega_m) = 0.044$. For the conservative lensing data quality equivalent to $\delta\gamma \sim 0.04$, the sample of 40 lenses constraints H_0 with 1.3% uncertainty. The parameter uncertainties are estimated for o Λ CDM model to be $\sigma(H_0) = 1.6\%$, $\sigma(\Omega_m) = 0.089$, and $\sigma(\Omega_K) = 0.12$ and for wCDM model to be $\sigma(H_0) = 2.9\%$, $\sigma(\Omega_m) = 0.05$, and $\sigma(w) = 0.22$. For N_{eff} CDM model, we estimate the parameter uncertainties to be $\sigma(H_0) = 0.93\%$, $\sigma(\Omega_m) = 0.045$. Adding more lens to the sample does not improve the degeneracy in N_{eff} showing time-delay cosmography is insensitive to N_{eff} .

For the owCDM model, we estimate the parameter uncertainties to be $\sigma(H_0) = 3.6\%$, $\sigma(\Omega_m) = 0.17$, $\sigma(\Omega_K) = 0.21$, $\sigma(w) = 0.42$. For the w_a CDM model, w_0 and w_a are estimated with uncertainties $\sigma(w_0) = 0.55$ and $\sigma(w_a) = 3.0$, respectively.

5.2 Joint analysis with *Planck*

We combined the inference on cosmography from strong lensing with *Planck* 2015 data release (Planck Collaboration et al. 2016, hereafter *Planck*).² To combine the two datasets, we followed the importance sampling method prescribed by Lewis & Bridle (2002) and implemented by Suyu et al. (2010, 2013), and Bonvin et al. (2017). We used the bivariate normal distribution fit of the posterior PDF of D_d and $D_{\Delta t}$ given in Equation (33) to compute the “importance” or weight of each point in the *Planck* chain.

For many combinations of cosmological model and parameters, the confidence regions from the time-delay cosmography are orthogonal to the ones from the *Planck*. As a result, combining the inferences from the time-delay cosmography with the *Planck* leads to much tighter constraints (Figure 10).

For flat Λ CDM model, combining *Planck* with nine lenses leads to an 1.1% measurement of H_0 . For the combination of 40 lenses and *Planck*, the precision of H_0 becomes 0.74% (Table 7) in the flat Λ CDM model.

For o Λ CDM model, the maximum likelihood regions of the *Planck* and the lensing data with the “primary” fiducial

² We used the *Planck* chains designated by “plikHM_TT_lowTEB” which uses the baseline high-l *Planck* power spectra and low-l temperature and LFI polarization.

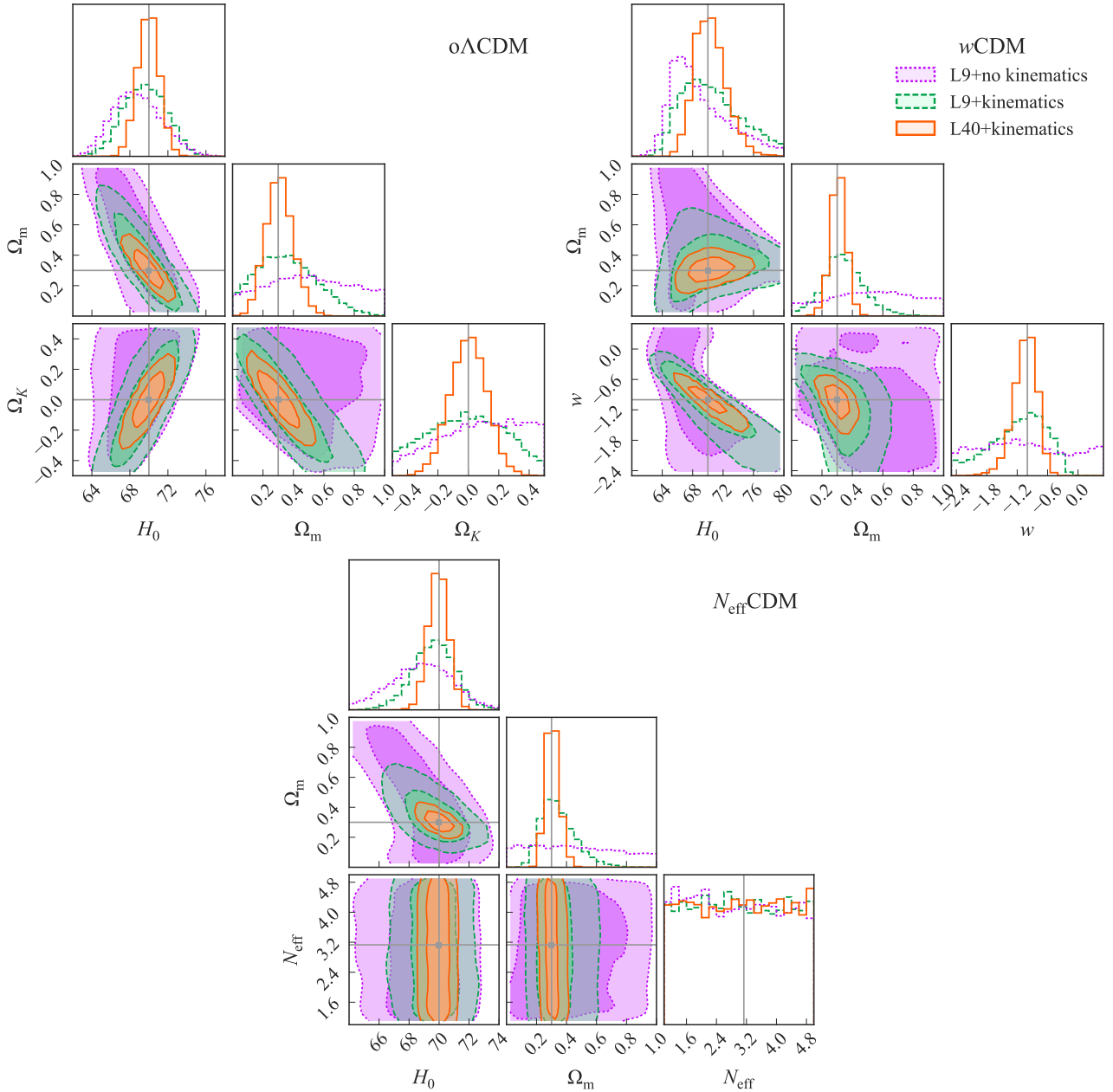


Figure 8. Posterior PDF of cosmological parameters obtained from distance measurements for Λ CDM (top left), w CDM model (top right), and N_{eff} CDM (bottom) models. The posterior PDF inferred from nine lenses (L9) without kinematics is shown in dotted contours, from nine lenses with kinematics is shown in dashed contours, and from 40 lenses (L40) with kinematics is shown in solid contours. The contours represent 1σ and 2σ confidence regions. Solid straight lines show the fiducial values. For all cosmological models, adding spatially resolved kinematics lifts degeneracies between the cosmological parameters and puts tighter constraints on them.

cosmology are too far apart to implement the importance sampling method. Therefore, we used the *Planck* values, $H_0 = 56.5$ km/s/Mpc, $\Omega_m = 0.441$, $\Omega_\Lambda = 0.592$, $\Omega_K = -0.033$ as the fiducial cosmology to generate the lensing likelihood to combine with the *Planck* likelihood. This combination gives $\sigma(H_0) = 1.8\%$, $\sigma(\Omega_m) = 0.017$, and $\sigma(\Omega_K) = 0.0048$ for nine lenses and $\sigma(H_0) = 0.81\%$, $\sigma(\Omega_m) = 0.01$, and $\sigma(\Omega_K) = 0.0031$ for 40 lenses.

For the w CDM model, the precision of w is estimated to be $\sigma(w) = 0.081$ and $\sigma(w) = 0.060$ for combination of *Planck* with nine and 40 lenses, respectively. For the N_{eff} CDM

model, we constrain the number of relativistic species with $\sigma(N_{\text{eff}}) = 0.16$ and $\sigma(N_{\text{eff}}) = 0.13$ by combining *Planck* with nine and 40 lenses, respectively.

We did not combine *Planck* with the lensing likelihoods for Λ CDM model as the *Planck* collaboration did not publicly release the parameter chains for this model. For w_a CDM model, we combined the lensing information with *Planck*+BAO constraints. From the joint analysis, we estimate the parameter uncertainties to be $\sigma(w_0) = 0.29$ and $\sigma(w_a) = 0.86$ giving dark-energy figure of merit (FoM, given by the inverse of the area enclosed by the 1σ confidence

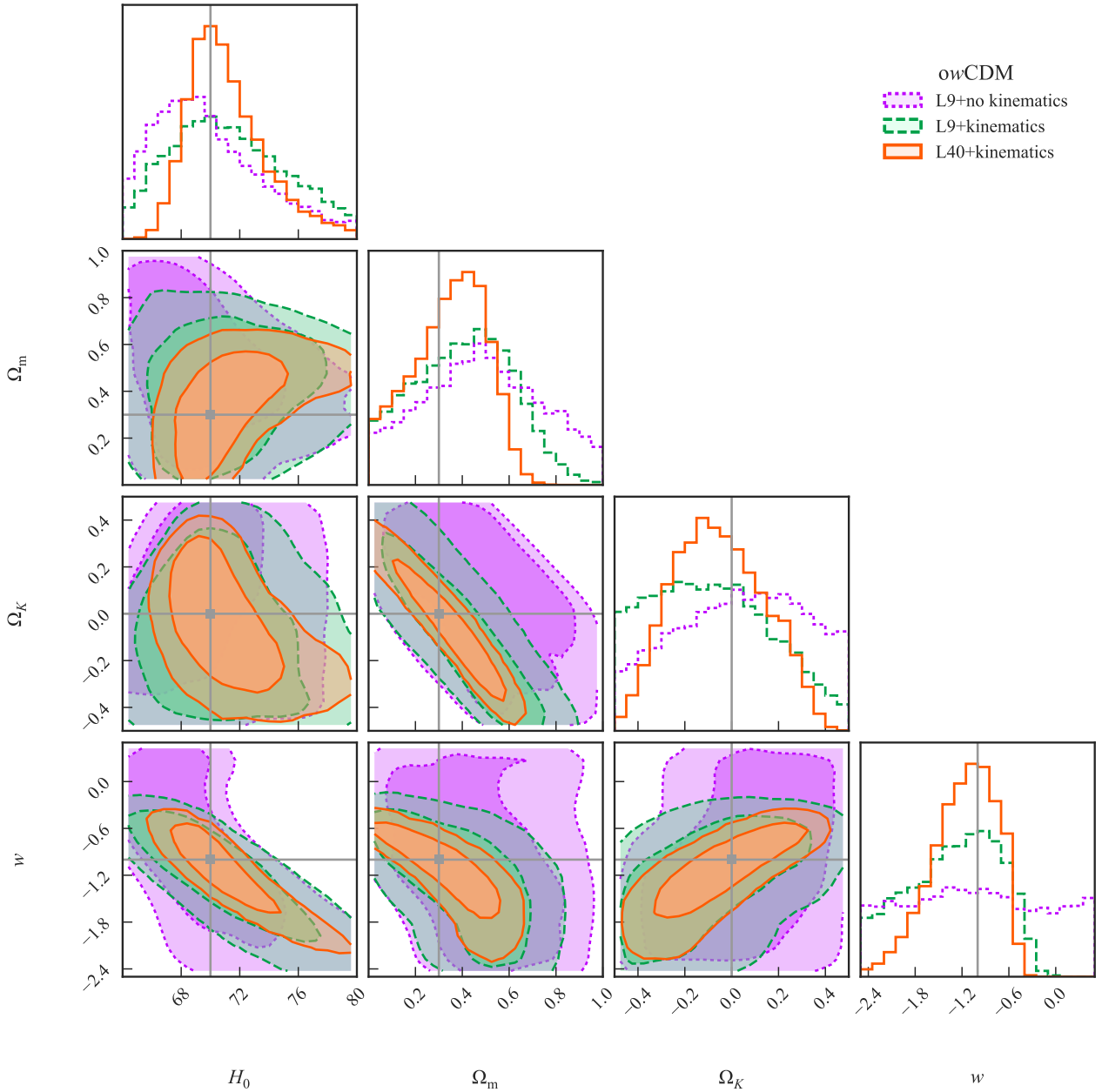


Figure 9. Posterior PDF of cosmological parameters obtained from the distance measurements for owCDM model. The posterior PDF inferred from nine lenses (L9) without kinematics is shown in dotted contours, from nine lenses with kinematics is shown in dashed contours, and from 40 lenses (L40) with kinematics is shown in solid contours. The contours represent 1σ and 2σ confidence regions. Solid straight lines show the fiducial values. This is a further illustration of the role of spatially resolved kinematics in breaking degeneracies between the parameters for a two-parameter extension from the basic Λ CDM model.

contour in the $w_0 - w_a$ plane) 0.85 for nine lenses, and $\sigma(w_0) = 0.27$ and $\sigma(w_a) = 0.82$ giving an FoM = 1.11 for 40 lenses.

6 DISCUSSION AND COMPARISON WITH PREVIOUS WORK

We explored how incorporating spatially resolved kinematics of the deflector in addition to the lensing and time-delay data improves the precision of the inferred cosmological pa-

rameters. We showed that the addition of the spatially resolved kinematics to the lensing and time-delay data helps break the mass-anisotropy degeneracy and leads to improved precision in the determination of the angular diameter distance of the deflector (from $\sim 20\%$ to $\sim 10\%$). We found that the time-delay distances can be simultaneously measured with $\sim 6\%$ accuracy, which is comparable to the 6% measurement of the time-delay distance for the lens RXJ1131-1231 (Suyu et al. 2013) and the 7.6% measurement for the lens HE0435-1223 (Wong et al. 2017). These precision margins are achievable by current and future IFs, e.g. OSIRIS on

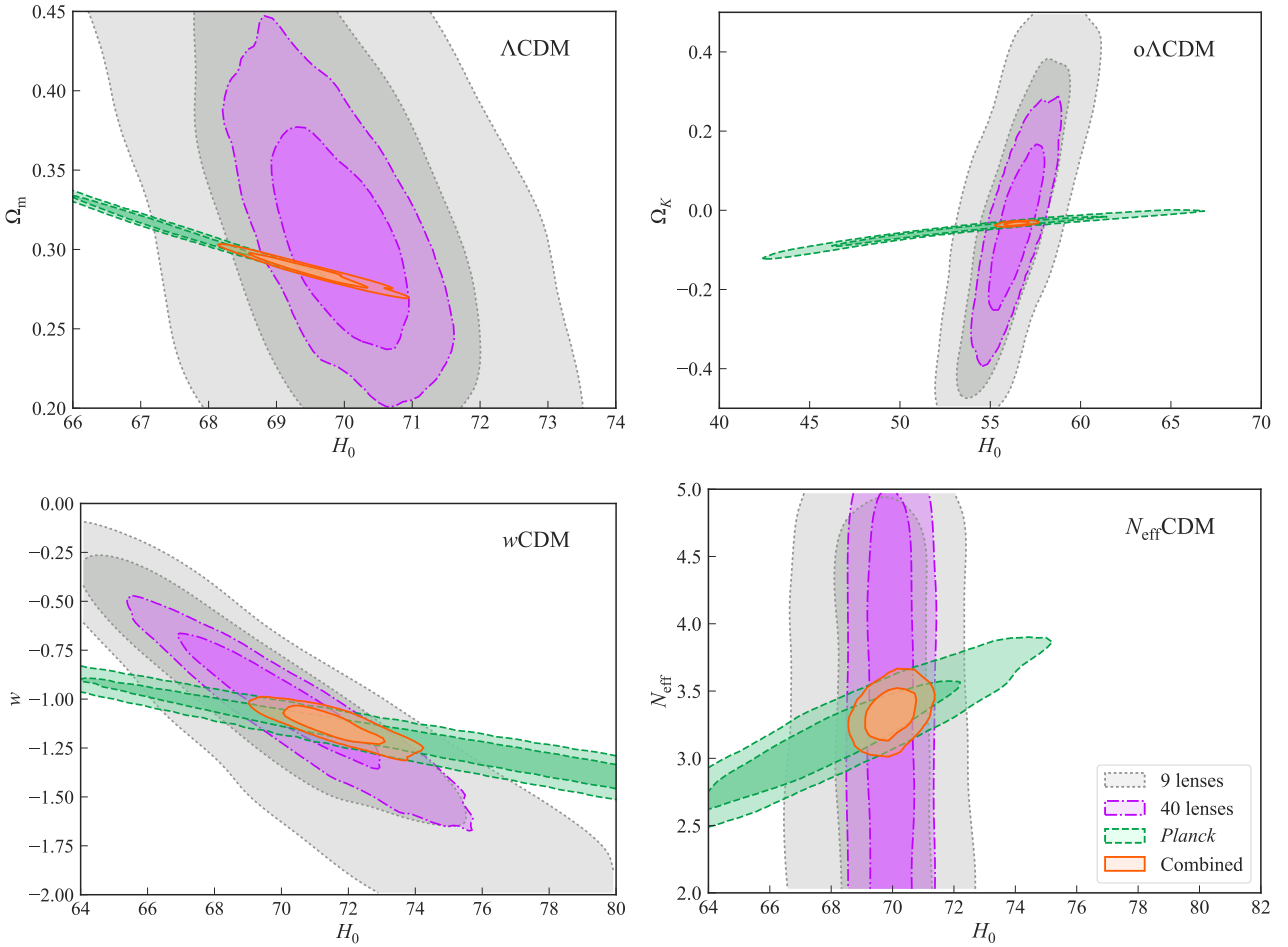


Figure 10. 1σ and 2σ regions of cosmological parameters obtained from lensing data alone and in combination with *Planck* for Λ CDM (top left), $o\Lambda$ CDM (top right), w CDM (bottom left), and N_{eff} CDM (bottom right) models. The constraints from nine lenses with spatially resolved kinematics are shown with dotted contours, from 40 lenses with spatially resolved kinematics are shown with dash-dotted contours, from *Planck* are shown in dashed contours, and from the combination of *Planck* and 40 lenses are shown in solid contours. In all cases, adding the lensing information to the *Planck* data improves the constraints on the cosmological parameters.

Keck with laser guide star AO or space-based instruments, e.g. NIRSPEC on JWST. Future telescopes like TMT or E-ELT would improve these precisions further. Jee et al. (2016) assume 5% precision on both angular diameter and time-delay distances, however we found that 5% precision on angular diameter distance measurement is probably beyond reach with current or imminent technology.

We confirmed the result by Linder (2011) and Jee et al. (2016) that combining lensing information with CMB and other external datasets can greatly improve the constraints on the cosmological parameters. Linder (2011) finds that by combining time-delay distance measurements with 5% uncertainty from 150 hypothetical strong lens systems with the CMB and supernova constraints, dark energy figure of merit can be improved by almost a factor of 5. Jee et al. (2016) find that combining angular diameter and time-delay distance measurements with 5% uncertainties on both from 55 lenses with *Planck*+BAO+JLA constraints improves the precision on w_a and the dark energy figure of merit by approximately a factor of two for the time-varying dark energy model. In our study, combining angular diameter and time-delay distance measurements with $\sim 10\%$ and $\sim 6\%$ un-

certainties, respectively, from 40 lenses with *Planck*+BAO data improves the *Planck*+BAO constraint on w_a by 13% and the dark energy figure of merit by 56%, consistent with previous results after taking into account the differences.

7 LIMITATION OF THIS PRESENT WORK

In order to model a large number of lenses in a computationally efficient manner we adopted many simplifying assumptions. First, we used a collection of conjugate points to replace the detailed modeling of the lensed quasar host galaxy. Second, we assumed spherical symmetry to speed up the calculations. By requiring the uncertainty on the effective mass density profile slope to be equal to 0.02, the precision obtained by full-blown models, this procedure ensures that we get realistic uncertainties on distances. We know from full pixel based simulations that such precision can be attained by modeling images obtained with reasonable exposure time using current and future technology (Meng et al. 2015). A similar study is required to estimate the exposure times re-

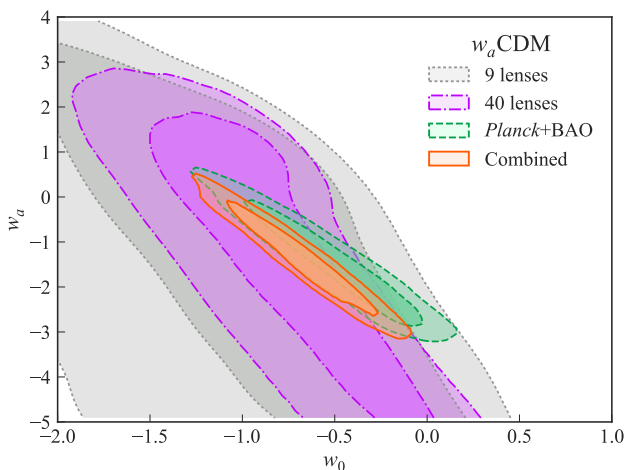


Figure 11. 1σ and 2σ confidence regions of the dark energy equation of state parameters obtained from lensing data alone and in combination with *Planck* for w_a CDM model. The constraints from nine lenses with spatially resolved kinematics are shown with dotted contours, from 40 lenses with spatially resolved kinematics are shown with dash-dotted contours, from *Planck* are shown in dashed contours, and from the combination of *Planck* and 40 lenses are shown in solid contours. Adding lensing measurements to the *Planck*+BAO data improves the dark energy figure of merit by 56%.

quired to carry out the spectroscopic observations (Meng et al. 2017, in prep).

We assumed a 3-5% uncertainty for the external convergence as it can be indirectly estimated by comparing the statistics of galaxy number counts along the line of sight with simulated light cones from the Millennium Simulation. This approach has the caveat of being dependent on the assumed cosmology and thus possibly biasing the final cosmological inferences (Rusu et al. 2017). Moreover, there can be $\sim 25\%$ deviation in the inferred κ_{ext} between the *Planck* cosmology and the Millennium Simulation. This would leave some residual systematics to be accounted for when analyzing real-life lenses. With the most pessimistic approach of 25% variation between median κ_{ext} inferred from ray-tracing, this would mean that a median value of $\kappa_{\text{ext}} = 0.04$ would impart a 1% systematic uncertainty on H_0 . However, κ_{ext} can be shown to depend primarily on $\Omega_m \sigma_8$ where σ_8 is the root-mean-square fluctuation of the mass density, while other contributions are sub-dominant (Equation C4 in Rusu et al. 2017). This means that one can perform a complete cosmographic inference, where also Ω_m and σ_8 are varied when importance-sampling from the CMB chains. Whereas the product $\Omega_m \sigma_8$ (hence the reconstructed median κ_{ext}) can vary appreciably between “different” CMB experiments (with different setups, or different multipole coverage, or beam characterization), its possible variation is smaller within the same CMB experiment, which means that the median κ_{ext} inferred will vary by less than the most pessimistic estimate (25% to 1% on H_0). Hence, regardless of whether $\Omega_m \sigma_8$ are varied or kept at a fiducial value when considering κ_{ext} , time-delays are still a robust way of probing departures from flat- Λ CDM as inferred from within a particular CMB probe, without particular worries from the κ_{ext} reconstruction, with sub-

percent accuracy. There are, in fact, other factors affecting the accuracy of κ_{ext} reconstruction, such as the choice of weighting scheme in terms of distances and masses, or the importance of a multi-plane approach. However, when dealing with real-life lenses, these have been (and are being) discussed at length for each individual system while still at blinded-inference stage. Different lenses have required different evaluations of κ_{ext} , but after unblinding they have all given consistent H_0 results, which suggests that this side of reconstruction systematics is currently under control. Part of the reason may be that the width of the κ_{ext} PDF is not negligible with respect to the median, so any systematics affecting the shift in κ_{ext} are still comprised within 1σ from the “true” value.

Finally, we emphasize that our study takes into account systematic uncertainties only in an indirect manner. Possible sources of known systematics can be contamination from the bright quasar images to the the host galaxy flux or the deflector spectra, unaccounted line-of-sight contribution to the projected mass etc. We assumed that these sources of known systematics can be accounted by our chosen error budget for different mock data and model parameters, e.g. 5-10% uncertainty on the velocity dispersion and 3-5% uncertainty on the external convergence, which are realistic error budgets for these quantities from the state of the art measurements. It would be useful to carry out a systematic investigation of strategies that may be required to limit any potential bias arising from these systematic uncertainties to be well below the statistical errors.

8 SUMMARY

Strong lenses with measured time delays can be used as probes to constrain cosmological parameters through the measurement of the angular diameter distance to the deflector and the time-delay distance. However, spatially resolved kinematics is essential to measure the angular diameter distance to the deflector and it also helps break the mass-anisotropy degeneracy. In this paper, we used a realistic model of a deflector galaxy to create mock lensing and kinematic data and estimated the achievable precisions of the cosmological parameters. The main conclusions of this study are as follow:

- The angular diameter distance to the deflector can be measured to approximately 10% uncertainty by including spatially resolved kinematics from current ground-based IFS with laser guide star AO, e.g. OSIRIS on Keck, or with space-based instruments, e.g. NIRSPEC on JWST, to the imaging data of the lensed quasar and the time delay measurement. The time-delay distance can be simultaneously measured to $\sim 6\%$ uncertainty.
- Using spatially resolved kinematics improves the precision on angular diameter distance per system from $\sim 20\%$ to $\sim 10\%$ over using integrated kinematic data.
- H_0 can be measured to 2.0% precision using lensing and spatially resolved kinematics from nine lenses and to sub-percent precision (0.9%) from 40 lenses.
- The uncertainty on H_0 improves from 3.2 to 2.0% by adding the spatially resolved kinematics to the lensing and time-delay data for nine strong lens systems.

• Combining *Planck* with lensing and spatially resolved kinematics data can break degeneracies between the cosmological parameters and greatly improve the constraints on them. Especially, for the time-dependent dark energy parameter model, the dark energy figure of merit is improved by 56% by combining a sample of 40 lenses with measured time delays and kinematics with *Planck*+BAO constraints.

This is a very interesting time for time-delay cosmography as several wide-field and deep-sky surveys such as the Dark Energy Survey, Euclid, the Wide Field Infrared Survey Telescope (WFIRST), the Large Synoptic Survey Telescope (LSST), should allow for the discovery and follow-up of tens to hundreds of multiply imaged quasars (Oguri & Marshall 2010). The launch of NIRSPEC on JWST, scheduled for 2018, and the constantly improving ground-based instruments with laser guide star AO (e.g. OSIRIS on Keck) make it possible to have high-quality spatially resolved kinematics for these lens systems. In turn, this can lead to the measurement of the Hubble parameter to sub-percent precision. Combining the distance measurements from strong lens systems to other cosmological probes, i.e. CMB, BAO, and type Ia supernova, would help tightly constraint the cosmological parameters leading to a deeper understanding of dark energy, dark matter, and other fundamental properties of our Universe.

ACKNOWLEDGMENT

We thank Simon Birrer, Inh Jee, Eiichiro Komatsu, Philip J. Marshall, Sherry H. Suyu, and Xin Wang for many insightful conversations. We also thank the anonymous referee whose comments helped us to improve this work. AS and TT acknowledge support by the Packard Foundation through a Packard Research Fellowship and by the National Science Foundation through grant AST-1450141. This work used computational and storage services associated with the Hoffman2 Shared Cluster provided by UCLA Institute for Digital Research and Education's Research Technology Group. This research made use of Astropy, a community-developed core Python package for Astronomy (Astropy Collaboration et al. 2013), and the CORNER.PY code at <https://github.com/dfm/corner.py> (Foreman-Mackey 2016).

REFERENCES

- Agnello A., Auger M. W., Evans N. W., 2013, *MNRAS*, **429**, L35
- Agnello A., Evans N. W., Romanowsky A. J., 2014a, *MNRAS*, **442**, 3284
- Agnello A., Evans N. W., Romanowsky A. J., Brodie J. P., 2014b, *MNRAS*, **442**, 3299
- Akeret J., Seehars S., Amara A., Refregier A., Csillaghy A., 2013, *Astronomy and Computing*, **2**, 27
- Alam S., et al., 2016, preprint, ([arXiv:1607.03155](https://arxiv.org/abs/1607.03155))
- Astropy Collaboration et al., 2013, *A&A*, **558**, A33
- Auger M. W., Treu T., Bolton A. S., Gavazzi R., Koopmans L. V. E., Marshall P. J., Moustakas L. A., Burles S., 2010, *ApJ*, **724**, 511
- Barnabè M., Czoske O., Koopmans L. V. E., Treu T., Bolton A. S., 2011, *MNRAS*, **415**, 2215
- Bartelmann M., 1996, *A&A*, **313**, 697
- Bartelmann M., Meneghetti M., 2004, *A&A*, **418**, 413
- Bernal J. L., Verde L., Riess A. G., 2016, *J. Cosmology Astropart. Phys.*, **10**, 019
- Birrer S., Amara A., Refregier A., 2016, *J. Cosmology Astropart. Phys.*, **8**, 020
- Bonvin V., et al., 2017, *MNRAS*, **465**, 4914
- Brewer B. J., Marshall P. J., Auger M. W., Treu T., Dutton A. A., Barnabè M., 2014, *MNRAS*, **437**, 1950
- Collett T. E., et al., 2013, *MNRAS*, **432**, 679
- Courteau S., et al., 2014, *Reviews of Modern Physics*, **86**, 47
- Dutton A. A., Treu T., 2014, *MNRAS*, **438**, 3594
- Eisenstein D. J., et al., 2005, *ApJ*, **633**, 560
- Falco E. E., Gorenstein M. V., Shapiro I. I., 1985, *ApJ*, **289**, L1
- Foreman-Mackey D., 2016, *The Journal of Open Source Software*, **24**
- Foreman-Mackey D., Hogg D. W., Lang D., Goodman J., 2013, *PASP*, **125**, 306
- Gavazzi R., Treu T., Rhodes J. D., Koopmans L. V. E., Bolton A. S., Burles S., Massey R. J., Moustakas L. A., 2007, *ApJ*, **667**, 176
- Gavazzi R., Treu T., Koopmans L. V. E., Bolton A. S., Moustakas L. A., Burles S., Marshall P. J., 2008, *ApJ*, **677**, 1046
- Goodman J., Weare J., 2010, *Communications in Applied Mathematics and Computational Science*, **5**, 65
- Greene Z. S., et al., 2013, *ApJ*, **768**, 39
- Grillo C., Lombardi M., Bertin G., 2008, *A&A*, **477**, 397
- Hilbert S., Hartlap J., White S. D. M., Schneider P., 2009, *A&A*, **499**, 31
- Jaffe W., 1983, *MNRAS*, **202**, 995
- Jee I., Komatsu E., Suyu S. H., 2015, *J. Cosmology Astropart. Phys.*, **11**, 033
- Jee I., Komatsu E., Suyu S. H., Huterer D., 2016, *J. Cosmology Astropart. Phys.*, **4**, 031
- Kennedy J., Eberhart R., 1995, in Proceedings of ICNN'95 - International Conference on Neural Networks. IEEE, doi:10.1109/icnn.1995.488968, <https://doi.org/10.1109/icnn.1995.488968>
- Koopmans L. V. E., Treu T., Fassnacht C. D., Blandford R. D., Surpi G., 2003, *ApJ*, **599**, 70
- Koopmans L. V. E., Treu T., Bolton A. S., Burles S., Moustakas L. A., 2006, *ApJ*, **649**, 599
- Koopmans L. V. E., et al., 2009, *ApJ*, **703**, L51
- Larkin J., et al., 2006, *New Astron. Rev.*, **50**, 362
- Lewis A., Bridle S., 2002, *Phys. Rev. D*, **66**, 103511
- Linder E. V., 2011, *Phys. Rev. D*, **84**, 123529
- Mamon G. A., Lokas E. L., 2005, *MNRAS*, **363**, 705
- Meneghetti M., Bartelmann M., Moscardini L., 2003, *MNRAS*, **340**, 105
- Meng X.-L., Treu T., Agnello A., Auger M. W., Liao K., Marshall P. J., 2015, *J. Cosmology Astropart. Phys.*, **9**, 059
- Merritt D., 1985a, *AJ*, **90**, 1027
- Merritt D., 1985b, *MNRAS*, **214**, 25P
- Navarro J. F., Frenk C. S., White S. D. M., 1996, *ApJ*, **462**, 563
- Navarro J. F., Frenk C. S., White S. D. M., 1997, *ApJ*, **490**, 493
- Oguri M., Marshall P. J., 2010, *MNRAS*, **405**, 2579
- Osipkov L. P., 1979, *Pisma v Astronomicheskii Zhurnal*, **5**, 77
- Paraficz D., Hjorth J., 2009, *A&A*, **507**, L49
- Perlmutter S., et al., 1999, *ApJ*, **517**, 565
- Planck Collaboration et al., 2016, *A&A*, **594**, A13
- Refsdal S., 1964, *MNRAS*, **128**, 307
- Riess A. G., et al., 1998, *AJ*, **116**, 1009
- Riess A. G., et al., 2016, *ApJ*, **826**, 56
- Rusu C. E., et al., 2017, *MNRAS*, **467**, 4220
- Schneider P., Sluse D., 2013, *A&A*, **559**, A37
- Schneider P., Sluse D., 2014, *A&A*, **564**, A103
- Schneider P., Kochanek C. S., Wambsganss J., 2006, *Gravitational Lensing: Strong, Weak and Micro. Saas-Fee Advanced Courses Vol. 33*, Springer
- Sluse D., et al., 2016, *MNRAS*, submitted,

- Suyu S. H., 2012, *MNRAS*, **426**, 868
- Suyu S. H., Marshall P. J., Auger M. W., Hilbert S., Blandford R. D., Koopmans L. V. E., Fassnacht C. D., Treu T., 2010, *ApJ*, **711**, 201
- Suyu S. H., et al., 2012, preprint, ([arXiv:1202.4459](#))
- Suyu S. H., et al., 2013, *ApJ*, **766**, 70
- Suyu S. H., et al., 2014, *ApJ*, **788**, L35
- Treu T., Koopmans L. V. E., 2002a, *MNRAS*, **337**, L6
- Treu T., Koopmans L. V. E., 2002b, *ApJ*, **575**, 87
- Treu T., Koopmans L. V. E., 2004, *ApJ*, **611**, 739
- Treu T., Marshall P. J., 2016, preprint, ([arXiv:1605.05333](#))
- Weinberg D. H., Mortonson M. J., Eisenstein D. J., Hirata C., Riess A. G., Rozo E., 2013, *Phys. Rep.*, **530**, 87
- Wong K. C., et al., 2017, *MNRAS*, **465**, 4895
- Wright S. A., et al., 2016, in Society of Photo-Optical Instrumentation Engineers (SPIE) Conference Series. p. 990905 ([arXiv:1608.01696](#)), doi:10.1117/12.2233182
- Wucknitz O., 2002, *MNRAS*, **332**, 951
- Xu D., Sluse D., Schneider P., Springel V., Vogelsberger M., Nelson D., Hernquist L., 2016, *MNRAS*, **456**, 739
- van der Marel R. P., 1994, *MNRAS*, **270**, 271

This paper has been typeset from a $\text{\TeX}/\text{\LaTeX}$ file prepared by the author.

Table 7. Uncertainties on cosmological parameters

Datasets	H_0 (km/s/Mpc)	$\sigma(H_0)$ (%)	Ω_m	$\sigma(\Omega_m)$	Ω_k	$\sigma(\Omega_k)$	w	$\sigma(w)$	N_{eff}	$\sigma(N_{\text{eff}})$
Λ CDM										
L9*	69.7 ± 1.4	2.0	$0.33^{+0.09}_{-0.12}$	0.11	-	-	-	-	-	-
L40*	69.91 ± 0.64	0.92	$0.307^{+0.042}_{-0.047}$	0.044	-	-	-	-	-	-
L9+ <i>Planck</i>	$68.35^{+0.82}_{-0.73}$	1.1	0.300 ± 0.010	0.010	-	-	-	-	-	-
L40+ <i>Planck</i>	$69.45^{+0.59}_{-0.43}$	0.74	$0.2866^{+0.0058}_{-0.0061}$	0.0059	-	-	-	-	-	-
o Λ CDM										
L9	69.6 ± 2.3	3.3	$0.35^{+0.19}_{-0.22}$	0.20	-0.01 ± 0.27	0.27	-	-	-	-
L40	70.0 ± 1.1	1.6	$0.308^{+0.087}_{-0.091}$	0.089	0.00 ± 0.12	0.12	-	-	-	-
L9+ <i>Planck</i> [†]	$56.3^{+1.1}_{-0.9}$	1.8	$0.443^{+0.018}_{-0.016}$	0.017	-0.0341 ± 0.0048	0.0048	-	-	-	-
L40+ <i>Planck</i> [†]	$56.47^{+0.44}_{-0.47}$	0.81	$0.441^{+0.011}_{-0.009}$	0.010	$-0.0337^{+0.0033}_{-0.0030}$	0.0031	-	-	-	-
w CDM										
L9	$70.2^{+3.5}_{-4.3}$	6.2	$0.34^{+0.12}_{-0.13}$	0.13	-	-	$-1.11^{+0.66}_{-0.48}$	0.57	-	-
L40	$70.2^{+1.8}_{-2.2}$	2.9	0.307 ± 0.050	0.050	-	-	$-1.03^{+0.24}_{-0.21}$	0.22	-	-
L9+ <i>Planck</i>	$71.9^{+2.1}_{-1.8}$	2.8	$0.276^{+0.014}_{-0.015}$	0.015	-	-	-1.157 ± 0.081	0.081	-	-
L40+ <i>Planck</i>	$71.50^{+0.96}_{-0.79}$	1.2	$0.2779^{+0.0060}_{-0.0058}$	0.0059	-	-	$-1.127^{+0.054}_{-0.067}$	0.060	-	-
N_{eff} CDM										
L9	$69.7^{+1.4}_{-1.3}$	2.0	$0.33^{+0.09}_{-0.13}$	0.11	-	-	-	-	$3.0^{+1.3}_{-1.4}$	1.4
L40	69.94 ± 0.65	0.93	$0.305^{+0.042}_{-0.047}$	0.045	-	-	-	-	3.0 ± 1.4	1.4
L9+ <i>Planck</i>	$69.7^{+1.1}_{-1.0}$	1.6	$0.299^{+0.011}_{-0.010}$	0.010	-	-	-	-	3.31 ± 0.16	0.16
L40+ <i>Planck</i>	$69.94^{+0.55}_{-0.54}$	0.77	$0.2971^{+0.0084}_{-0.0076}$	0.0080	-	-	-	-	$3.33^{+0.13}_{-0.12}$	0.13
owCDM										
L9	$71.1^{+4.0}_{-5.2}$	6.5	$0.41^{+0.24}_{-0.20}$	0.22	$-0.10^{+0.26}_{-0.29}$	0.28	$-1.25^{+0.72}_{-0.55}$	0.63	-	-
L40	$70.7^{+2.0}_{-3.1}$	3.6	$0.36^{+0.19}_{-0.14}$	0.17	$-0.06^{+0.19}_{-0.22}$	0.21	$-1.14^{+0.46}_{-0.38}$	0.42	-	-
w_a CDM										
Datasets	H_0 (km/s/Mpc)	$\sigma(H_0)$ (%)	Ω_m	$\sigma(\Omega_m)$	Ω_Λ	$\sigma(\Omega_\Lambda)$	w_0	$\sigma(w_0)$	w_a	$\sigma(w_a)$
L9	$70.4^{+5.0}_{-5.8}$	7.7	$0.40^{+0.12}_{-0.13}$	0.13	$0.60^{+0.12}_{-0.13}$	0.13	$-0.98^{+0.86}_{-0.77}$	0.82	$-2.2^{+3.7}_{-3.3}$	3.5
L40	$68.7^{+3.7}_{-3.6}$	5.3	$0.359^{+0.092}_{-0.078}$	0.085	$0.641^{+0.092}_{-0.078}$	0.085	$-0.77^{+0.46}_{-0.64}$	0.55	$-1.6^{+2.4}_{-2.4}$	3.0
L9+ <i>Planck</i> +BAO	$65.5^{+2.6}_{-2.2}$	3.7	0.335 ± 0.025	0.025	0.665 ± 0.025	0.025	$-0.59^{+0.28}_{-0.29}$	0.29	$-1.46^{+0.86}_{-0.85}$	0.86
L40+ <i>Planck</i> +BAO	$67.0^{+2.2}_{-2.0}$	3.2	$0.321^{+0.022}_{-0.020}$	0.021	$0.679^{+0.020}_{-0.022}$	0.021	$-0.67^{+0.23}_{-0.26}$	0.25	$-1.39^{+0.75}_{-0.77}$	0.76

* L9 refers to the set of nine lenses and L40 refers to the set of 40 lenses.

[†] For o Λ CDM model, to combine *Planck* with the lensing information, the fiducial cosmology was chosen to be the *Planck* o Λ CDM cosmology: $H_0 = 56.5$ km/s/Mpc, $\Omega_m = 0.441$, $\Omega_\Lambda = 0.592$, and $\Omega_K = -0.033$.